

AN ABSTRACT OF THE THESIS OF

Justina A. M. Freilich for the degree of Master of Science in Radiation Health Physics presented on March 15, 2021.

Title: Effects of MCNP Model Resolution on Predicting Water Equivalent Thickness of Nanocomposite Materials in High-Energy Proton Fields

Abstract approved: _____

Camille J. Palmer

Manned missions beyond low-Earth orbit present tremendous, multifaceted radiological challenges. The deep space radiation environment contains high-energy protons and heavy ions, which are not sufficiently shielded by the aluminum alloys that have historically been used in spacecraft. To address these shielding concerns, polymer-based nanocomposites have been proposed. Radiation transport simulations of these nanocomposite materials could reduce the lead time for materials development, however, the level of detail necessary in a model to accurately predict the water equivalent thickness (WET) of a nanoscale material is unknown. In this work, MCNP6.2 is used to simulate the transport of high-energy protons through several models, varying three parameters (experimental setup geometry, particle tracking physics, and nanocomposite geometry), and the results are compared to available experimental measurements. The MCNP results indicate that the inclusion of δ -ray production in the particle tracking physics alters both the magnitude of the Bragg peak and the simulated proton range. Altering the other two parameters showed less than a 1% change in proton range, which is within the statistical error. The simulated WET of the nanocomposite, modeled as a bulk homogeneous material, was comparable to the published experimental results, with a WET of 44.70 mm in a 105 MeV proton beam and 22.61 mm in a 63MeV proton beam, and computed/experimental ratios of 0.9572 and 1.025, respectively.

©Copyright by Justina A. M. Freilich
March 15, 2021
All Rights Reserved

Effects of MCNP Model Resolution on Predicting Water Equivalent Thickness of
Nanocomposite Materials in High-Energy Proton Fields

by
Justina A. M. Freilich

A THESIS

submitted to

Oregon State University

in partial fulfillment of
the requirements for the
degree of

Master of Science

Presented March 15, 2021
Commencement June 2021

Master of Science thesis of Justina A. M. Freilich presented on March 15, 2021.

APPROVED:

Major Professor, representing Radiation Health Physics

Head of the School of Nuclear Science and Engineering

Dean of the Graduate School

I understand that my thesis will become part of the permanent collection of Oregon State University libraries. My signature below authorizes release of my thesis to any reader upon request.

Justina A. M. Freilich, Author

ACKNOWLEDGEMENTS

I would like to express my sincere appreciation for Dr. Camille Palmer, for her patience and assistance through this project, and for helping me grow as a researcher and as a person. I am particularly grateful for her guidance and flexibility during this very strange year of academics and research.

I would also like to thank my other committee members, Dr. Lily Ranjbar, Dr. Samuel Briggs, and Dr. Leah Minc, for their time and input.

Thank you to the Oregon State University School of Nuclear Science and Engineering for their financial support through the Henry W. & Janice J. Schuette Graduate Fellowship and to Connie and Carl Clark and the ARCS Foundation Oregon Chapter for their financial support through the Connie L. & Carl J. Clark Scholarship.

Thank you to the friends I made at Oregon State University for welcoming me with open arms. I very much look forward to seeing what each of your bright minds brings to the world throughout your careers.

Thank you to my friends and family for supporting me through the countless *'I can't do it's* and for celebrating the *'I did it's* with me. Special thank you to Tyler for being a constant calming presence in my life.

Finally, thank you to Raymond Bowerman for first inspiring me to follow this path and to Oaklee Iris for inspiring me to continue.

TABLE OF CONTENTS

	<u>Page</u>
1 Introduction.....	1
1.1 Overview.....	1
1.2 Objectives	3
2 Background.....	4
2.1 History of Space Exploration.....	4
2.2 Deep Space Radiation Environment	5
2.3 Proton Transport Physics	9
2.4 Radiation Shielding Materials.....	13
2.5 Radiation Transport Modeling.....	16
3 Methods.....	20
3.1 Li <i>et. al.</i> Experimental Data.....	20
3.1.1 Overview.....	20
3.1.2 Materials	22
3.1.3 TRIUMF BL2C Setup.....	23
3.2 MCNP Input.....	24
3.2.1 Experimental Setup Geometry	24
3.2.2 Physics Settings	25
3.2.3 Nanocomposite Geometry	26
3.2.4 Tally Specification	29
3.3 Python Scripts	30
3.3.1 Input File Generation	31

TABLE OF CONTENTS (Continued)

3.3.2	MCNP Run Command.....	32
3.3.3	Data Extraction	32
4	Results & Discussion	34
4.1	Experimental Setup Results	34
4.2	Physics Parameter Results	35
4.3	Nanocomposite Geometry Results.....	36
4.4	Experimental Comparison	37
5	Conclusion	40
	Bibliography	42
	Appendices.....	49
Appendix A	SRIM Output for Hydrogen in Brass	50
Appendix B	MCNP Input Decks	51
Appendix C	Nanotube Modeler	53
Appendix D	Python Scripts	54

LIST OF FIGURES

<u>Figure</u>		<u>Page</u>
Figure 2.1	Stanley Peterson (left) and Raymond Bowerman (right) working on Intelsat I, the first commercial communications satellite, circa 1965	4
Figure 2.2	Plot of observed sunspot frequency over time, demonstrating the 11-year solar cycle	6
Figure 2.3	Red-bone-marrow-averaged absorbed dose as a function of aluminum shielding thickness and dose contribution source from a simulated GCR radiation environment using the FLUKA Monte-Carlo radiation transport code.....	7
Figure 2.4	Diagram of Van Allen belts relative to Earth’s magnetic and rotational axes	8
Figure 2.5	Dose rate data from the MSL Radiation Assessment Detector (RAD) during transit to Mars.....	9
Figure 2.6	Illustration of non-elastic nuclear interaction between a projectile proton (blue, left) and a target nucleus (green) resulting in target fragmentation	11
Figure 2.7	Plot of proton fluence (Φ) and dose (D) as a function of depth in a medium.....	12
Figure 2.8	Plot of experimental results showing a) tensile strength and b) flexural strength as functions of B ₄ C filler concentration in a high-density polyethylene matrix for microscale and nanoscale filler particles	14
Figure 2.9	Diagram of nanotube characteristics as they relate to a sheet of graphene (left) and illustrations of armchair and zigzag nanotubes (right)	15
Figure 2.10	Schematics of nanoparticles (NP) in a simple cubic motif (left) and a staggered motif (right)	18
Figure 3.1	Schematic showing the concept of water equivalent thickness	20
Figure 3.2	Simplistic diagram of the TRIUMF BL2C experimental setup used for proton irradiation testing.....	21

LIST OF FIGURES (Continued)

Figure 3.3	Complex diagram of the TRIUMF BL2C experimental setup used for proton irradiation testing.....	23
Figure 3.4	MCNP plot of the simplistic model (top) and complex model (bottom) of the experimental setup	24
Figure 3.5	MCNP plot of a carbon nanotube cross section (left) and the top view of a single carbon nanotube (right) using the hollow cylinder nanotube method.....	27
Figure 3.6	Angled view (left) and side view (right) of (18,2) nanotube in Nanotube Modeler software.....	28
Figure 3.7	MCNP plot of a carbon nanotube cross section (left) and the top view of a single carbon nanotube (right) using the atomistic nanotube method	28
Figure 3.8	Plot of quality factor as a continuous function of neutron energy from NCRP Report 38 and a point-wise function described in ICRP Publication 60	30
Figure 3.9	Image of a folder before (upper left) and after (upper right) running the expand.py script on it.....	31
Figure 3.10	Image of the folder after the folder_run.py script was used to run each input file through MCNP6.....	32
Figure 4.1	Comparison of BIC/DIC results for MCNP simulations of an aluminum sample in 63 MeV proton beam with a simplistic and complex experimental setup geometry.....	34
Figure 4.2	Comparison of BIC/DIC results for three different MCNP simulations of an aluminum sample in 63 MeV proton beam, each with different physics settings	35
Figure 4.3	Comparison of BIC/DIC results for MCNP simulations of three different nanocomposite models, each with a different model resolution, tracking only protons and neutrons.....	37
Figure 4.4	Experimental (dotted) and computational (solid) results of proton irradiation at 63 MeV and 105 MeV	38

LIST OF TABLES

<u>Table</u>		<u>Page</u>
Table 2.1	Table of the particle types and energies addressed in MCNP6 and their corresponding interaction physics	17
Table 3.1	Outline of each experiment performed, including beam energy, material, density, and sample thickness	22
Table 4.1	Experimental and computational results for each sample at each initial beam energy	39

LIST OF APPENDIX FIGURES

<u>Figure</u>		<u>Page</u>
Figure C.1	Screen capture of Nanotube Modeler software, showing nanotube characteristics and atom coordinates on the left and a 3D visual of the nanotube on the right	53
Figure D.1	Screen capture of Python script used to write input files with designated RS values	54
Figure D.2	Screen capture of Python script used to sequentially run MCNP6 for all .txt files within a designated folder.....	54
Figure D.3	Screen capture of Python script used to extract energy deposition data from MCNP output files within a designated folder	55

LIST OF ABBREVIATIONS

- BIC – background ion chamber
- CNT – carbon nanotube
- CSDA – continuous slowing-down approximation
- DIC – diagnostic ion chamber
- GCR – galactic cosmic ray
- HZE – high-Z and energy
- LEO – low-Earth orbit
- LET – linear energy transfer
- ISS – International Space Station
- MCNP – Monte Carlo N-Particle
- MSL – Mars Science Laboratory
- PDMS – polydimethylsiloxane
- RS – range shifter
- SPE – solar particle event
- SRIM – Stopping and Range of Ions in Matter
- SWCNT – single-walled carbon nanotube
- WET – water equivalent thickness

1 Introduction

1.1 Overview

As interest in space exploration grows, the length and complexity of planned missions tends to follow the same trend. While estimated timelines change frequently, a manned mission to Mars is likely to occur in the next several decades¹⁻³. The duration and distance-from-Earth of a Mars mission far exceed any previous manned expedition, which introduces new challenges. The increase in mission duration and distance necessitates the consideration of new health concerns facing the crew members chosen for these missions. A major health concern related to long-duration missions, particularly in deep space, is radiation exposure to crew members and the associated stochastic (e.g. cancer) and non-stochastic (e.g. cataracts) health effects⁴⁻¹⁰.

To mitigate the risks presented by the radiation present in deep space, appropriate radiation shielding is necessary. Historically, aluminum and aluminum alloys are the most commonly used shielding materials for manned spacecraft, as they are sufficient for manned missions that do not surpass low-Earth orbit, and provide structural stability in addition to some radiation protection¹¹⁻¹³. For missions beyond low-Earth orbit, however, aluminum is not a suitable shielding material for several reasons. The amount of aluminum needed to sufficiently shield from the incident radiation would be quite heavy and would, therefore, increase mission costs¹⁴. Additionally, when the high-energy particles found in deep space interact with a heavy material like aluminum, secondary radiation is produced, which poses a significant threat to crew safety^{10,13}.

Novel polymer-based nanocomposites have been proposed for use as multifunctional shielding, acting as both radiation shielding and a structural component of the spacecraft¹⁴. Materials with a high hydrogen content, like polymers, are known to shield protons and heavy ions with less secondary particle production than aluminum shielding¹³. However, in order to serve as both radiation shielding and a structural material for a spacecraft, increased structural properties are necessary, ideally with little or no increase in weight^{11,13,14}. For this reason, carbon nanotube (CNT) fillers are a promising candidate for nanocomposite shielding. CNTs have a high strength-to-weight

ratio, with measured specific strengths up to $50,000 \text{ kN}\cdot\text{m}\cdot\text{kg}^{-1}$ compared to stainless steel's specific strength of around $60 \text{ kN}\cdot\text{m}\cdot\text{kg}^{-1}$. This allows for significant improvements in structural and thermal performance with minimal increases in weight and secondary particle production compared to reference shielding materials¹⁵⁻¹⁹. Research has shown that certain nanocomposites efficiently shield high-energy proton radiation^{16,20-23}. However, the large number of variables to be considered – polymer composition, filler composition, filler size, polymer-to-filler ratio, etc. – and the limited availability of appropriate testing facilities make robust nanocomposite studies difficult to perform²⁴⁻²⁶.

An alternative method of evaluating nanocomposites for shielding applications is through radiation transport simulations. Predicting the shielding performance of a material through simulation can be far less expensive in terms of time, cost, and resources than physical measurements, and can be used to shorten a material's development lead time. The Monte Carlo N-Particle (MCNP) code is a well-established radiation transport code that uses repeated random sampling in order to estimate the behavior of particles of interest²⁷. MCNP has been used to simulate radiation transport through a vast range of bulk materials, but it is unclear how the level of detail included in a model affects the accuracy of radiation transport simulations through nanoscale materials. Despite the well-documented differences in thermal, mechanical, and electrical properties of CNTs and bulk carbon^{15,17,18}, it remains unknown how these nanostructures influence radiation transport in MCNP.

The goal of this research is to assess the MCNP model fidelity needed to replicate an established high-energy proton experiment involving nanoscale materials. This study looks at the effects of model granularity on the accuracy of predicted attenuation of high-energy protons by altering three model parameters: experimental setup geometry, particle tracking physics, and nanocomposite geometry. For each parameter, radiation transport is simulated for several models of varying complexity and the resulting average proton ranges are compared. Additionally, the simulated water equivalent thicknesses (WETs) of three shielding materials are compared to published experimental values in 63 MeV and 105 MeV proton beams. Filling this knowledge gap can inform future work involving

MCNP simulations of nanoscale materials in high-energy proton fields and provide an understanding of the level of detail necessary for similar applications.

1.2 Objectives

This research aims to simulate an experimental design involving nanoscale materials in a high-energy proton field at various levels of detail to correlate common geometry and physics parameters to changes in the accuracy of the simulation. The overarching goal of the project can be broken down into the following objectives:

- Use MCNP to simulate a published experimental setup to predict the stopping power and WET of high-energy protons at 63 and 105 MeV in three materials, including one on the nanoscale;
- Compare the WET and stopping power predictions from MCNP simulations to published experimental values and evaluate the cause of any discrepancies between the two; and
- Suggest the relative importance of structural precision and physics definitions in modeling nanoscale structures in high-energy proton environments.

2 Literature Review

2.1 History of Space Exploration

Space exploration has long been a hallmark of mankind, driven by both curiosity and utility. From revolutionizing communication through the development of satellites like Intelsat I, shown in Figure 2.1, to aweing the world by reaching the moon, man has recognized the plethora of opportunities and challenges that space presents. Whether for philosophical implications or technological progression, space has remained a topic of interest in many circles. Satellites, rovers, and the ongoing scientific work being done on the International Space Station have provided scientific insight for the next steps in manned space exploration. It is widely agreed upon that Mars is the next target for a manned mission. Several governments and enterprises have released publications indicating their interest in a manned mission to Mars, with astronauts reaching the red planet in the next several decades²⁸⁻³⁰.



Figure 2.1. Stanley Peterson (left) and Raymond Bowerman (right) working on Intelsat I, the first commercial communications satellite, circa 1965. (Image from Britannica³¹.)

To achieve the timelines set forth by these organizations for a manned mission to Mars, there are many financial, logistical, and technological hurdles that must be overcome. One of these challenges is adequately protecting crew from high levels of radiation exposure to minimize the associated health risks. Because the radiation environment in LEO is quite different from that of deep space, unique radiation shielding solutions are necessary for a mission beyond LEO. In order to design and develop solutions, we must first understand the deep space radiation environment.

2.2 Deep Space Radiation Environment

Shielding is an important consideration in any scenario where workers and/or equipment will potentially be exposed to radiation above background levels. In order to select appropriate shielding materials for an application, it is important to first understand the characteristics of the expected radiation environment. The biological risk presented by a radiation exposure scenario depends largely on the types of particles emitted and their respective energies, so it is necessary to understand the sources of the radiation environment. For deep space missions, there are two main sources of radiation that must be considered: galactic cosmic rays (GCRs), solar particle events (SPEs)^{4,6,13,32}.

GCRs are rays of radiation that originate outside of the solar system and consist of high-energy protons and high-energy heavy ions (HZE) as well as a relatively small number of electrons and positrons^{6,33,34}. Of the particles that make up GCRs, approximately 85% are protons with energies ranging from tens of MeV to 10^{12} MeV and an energy distribution that peaks around 10^3 MeV^{9,34-36}. Because of their energies, these protons and HZE particles are difficult to attenuate using shielding materials that have been historically used for spacecrafts. Even in a low Earth orbit (LEO) scenario like the International Space Station (ISS), where some radiation is attenuated and/or diverted by the Earth's radiation belts and atmosphere, GCRs contribute approximately half of the total radiation dose to crew members³⁶. The hazard presented by GCRs is even greater with the absence of Earth's atmosphere and geomagnetic field in deep space³⁷.

The second source of radiation in space, SPEs, are solar events in which shifts in the Sun's magnetic fields cause the expulsion of energetic charged particles, including protons, electrons, and some HZEs. These solar events are categorized as either solar flares, which occur on a time scale of minutes-to-hours, or coronal mass ejections, which occur over hours or days. While the severity of SPEs is characteristically unpredictable, the frequency follows a periodic 11-year solar cycle, with four years of high solar activity and seven years of relatively low solar activity³⁸⁻⁴⁰. The solar cycle, which is generally measured by the number of observed sunspots over time, can be seen in Figure 2.2⁴⁰. In addition to number of sunspots over time, the size of the solar flares and coronal loops also fluctuates according the solar cycle. Due to the changes in the solar wind, the flux of GCR particles correlates inversely with the solar cycle^{6,41}.

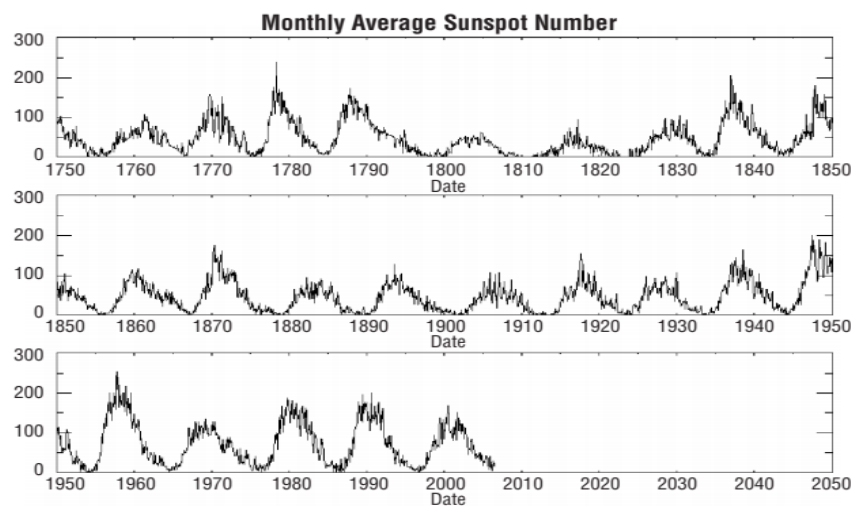


Figure 2.2. Plot of observed sunspot frequency over time, demonstrating the 11-year solar cycle. (Plot from Rask⁴⁰.)

When high-energy protons and ions from GCRs and SPEs interact with a medium, like a radiation shielding material or human tissue, they lose energy via several types of interactions. Most of their energy is lost in electromagnetic interactions, but incident particles may also undergo nuclear interaction. The latter occurs when a

projectile nucleus – a proton or HZE –elastically or inelastically collides with a target nucleus within the shielding material. In elastic nuclear collisions, the projectile nucleus is scattered, generally at a large angle. In inelastic nuclear collisions, either the projectile or target nucleus is split into smaller fragments, known as secondary particles^{42,43}. Nuclear fragmentation physics is discussed in greater detail in Section 2.3. Fragmentation of target nuclei can produce a multiplicity of secondary ions and neutrons that may contribute significantly to absorbed dose and pose a serious risk to crew members. The results of a computational study by Trovati, *et. al.* (2006) show the contribution of secondary particles to the absorbed dose, shown in Figure 2.3, in the red bone marrow of an anthropomorphic phantom in a GCR radiation environment with varying thicknesses of aluminum shielding⁴⁴. As the data shows, secondary radiation can contribute to a total dose nearly as much as primaries in the high-energy and high-atomic-number radiation environment of deep space.

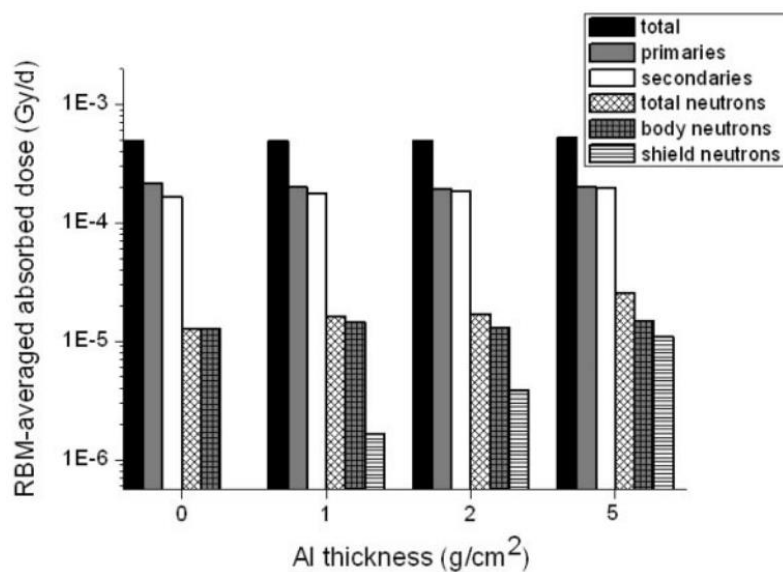


Figure 2.3. Red-bone-marrow-averaged absorbed dose as a function of aluminum shielding thickness and dose contribution source from a simulated GCR radiation environment using the FLUKA Monte-Carlo radiation transport code. (Plot from Trovati⁴⁴.)

There is an additional source of radiation that is often considered during space mission planning known as the Van Allen belts. The radiation belts consist primarily of energetic protons and electrons that are trapped in donut-shaped orbits by the Earth's magnetic field. The belts, shown in Figure 2.4, consists primarily of energetic protons and electrons that are trapped in donut-shaped orbits by the Earth's magnetic field. For LEO missions, the Van Allen belts can present a radiological hazard to crew if not shielded^{13,36,45}. Because of their proximity to Earth, consideration of the Van Allen belts is particularly important for missions in LEO. However, since deep space missions spend very little time passing through the Van Allen belts, they are not considered further in this work.

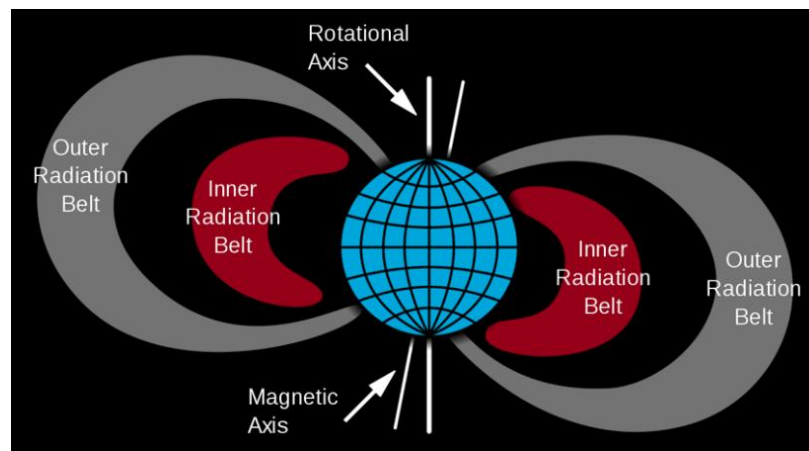


Figure 2.4. Diagram of Val Allen belts relative to Earth's magnetic and rotational axes. (Figure from NASA³⁹.)

The combined presence of these radiation sources creates a complex and sometimes volatile radiation environment, making it difficult to predict the dose rates crew members would experience during a manned mission. However, data collected from detectors in deep space can provide insight on the general range of doses that might be incurred. The Mars Science Laboratory (MSL), which launched in November 2011 and landed on the surface of Mars nine months later, collected dosimetric data during its travel to Mars and after landing. Dose rate data from the trip to Mars, as seen in Figure

2.5, shows the randomness and severity of the five SPEs that occurred during travel, corresponding to the five peaks in dose rate⁴⁶. The dose rate was shown to increase by as much as two orders of magnitude during SPEs compared to the relatively constant contribution from GCRs.

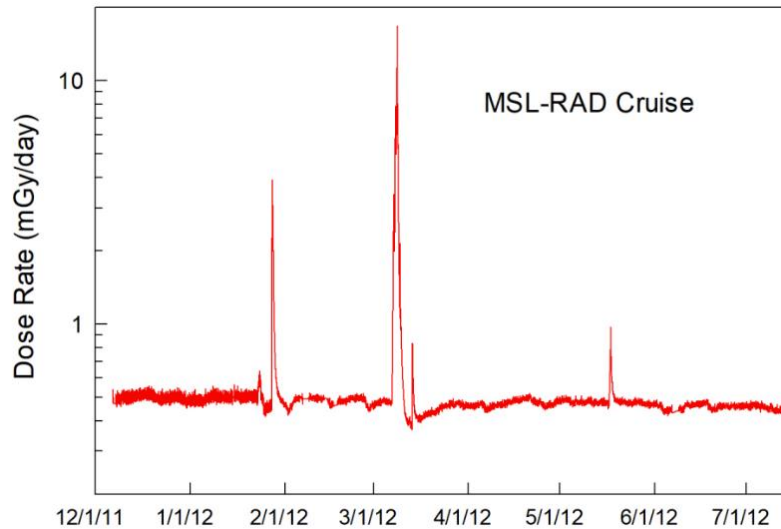


Figure 2.5. Dose rate data from the MSL Radiation Assessment Detector (RAD) during transit to Mars. (Plot from Simonsen⁴⁶.)

2.3 Proton Transport Physics

While the interaction of high-energy protons with novel materials like nanocomposites is a relatively new area of study, the dose profile of high-energy protons and ions with biological mediums like water and tissue has been well studied due to the prevalence of proton beam therapy for the treatment of cancers⁴⁷⁻⁵⁰. Though the application is quite different, the techniques used to characterize proton beams for therapeutic medicine is still useful for studying shielding materials and many of the same facilities are used for studies in both fields. The increased interest in finer localization of dose in radiation therapy over the past several decades has led to a wealth of literature discussing the fundamental physics involved in proton and ion transport through a medium⁵¹⁻⁵³.

The rate at which energy is lost is often measured as the linear energy transfer (LET), which describes the energy transferred from the particle to the surrounding medium per unit of distance traveled by the particle. Most of the energy lost by heavy charged particles is due to electromagnetic interactions between the incident particle and the electrons bonded to the atoms within the medium. Electromagnetic interactions result in either the excitation of an electron to a higher energy level or the ionization of the target atoms and small angle scattering of the incident particle, depending on the amount of energy transferred in the interaction and the binding energy of the electron^{42,51}. If enough energy is transferred during ionization, an electron known as a delta ray may escape its original orbit with enough remaining energy to cause secondary ionization as it travels⁵⁴. In addition to electromagnetic interactions, charged particles may also undergo nuclear interactions while traversing a medium, where the charged particle interacts with the nucleus of an atom within the medium.

Nuclear interactions can be categorized into elastic and inelastic nuclear collisions. Elastic nuclear collisions result in the large angle scattering of the projectile and target nuclei, while inelastic nuclear collisions cause fragmentation of the target nucleus, in the case of protons. If the projectile is a heavy ion, fragmentation can occur to the target nucleus, projectile nucleus, or both^{42,43}. Fragmentation and its effect on the dose equivalent within a spacecraft depend largely on which nucleus is fragmented – the target nucleus or the projectile nucleus. Target fragmentation caused by inelastic nuclear collisions can produce many secondary particles, emitted nearly isotropically, while projectile fragments only slightly deviate from the velocity and direction of the original charged particle. Additionally, projectile fragmentation is generally considered desirable in the sense of space radiation shielding, as it results in secondary radiation with lower LET than the original heavy ion.

Since LET is directly related to the quality factor, fragments with lower LET generally have lower quality factors than the higher atomic number projectile. In contrast, target fragmentation is often considered undesirable in deep space radiation shielding, as it can produce various types and energies of secondary radiation, as shown in Figure 2.6, that would not otherwise contribute to the dose, since the target projectile is assumed to

have no kinetic energy before the nuclear interaction takes place. In particular, the production of secondary neutrons can be problematic because they are uncharged and, therefore, do not lose energy via electromagnetic interaction. This means they only lose energy by interacting with nuclei, which may result in additional secondary particles with higher LET⁴³.

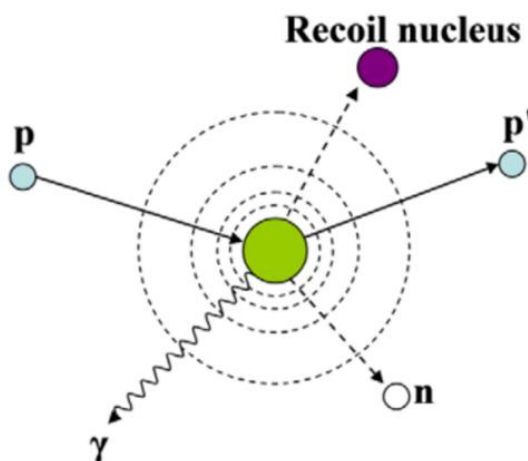


Figure 2.6. Illustration of non-elastic nuclear interaction between a projectile proton (blue, left) and a target nucleus (green) resulting in target fragmentation. (Figure from Newhauser⁵¹.)

Each of the interactions described above slow the projectile, whose LET is inversely proportional to the square of the projectile's velocity. Because of this relationship between velocity and energy transfer, protons deposit the greatest energy per unit length near the end of their range in a medium. When plotted as a function of depth in a medium, fluence shows a very slight linear decrease followed by a steep decline as the depth approaches the average proton range. The plot of dose as a function of depth shows a linear relationship in the region well below the proton range, followed by a peak as the majority of the protons, which have been slowed to a high-LET state, deposit the last of their energy^{42,47,51}. This peak in the dose-versus-depth plot, shown in Figure 2.7, is

known as the Bragg peak and is used to identify the mean particle range and the depth that will receive the greatest dose⁵⁵.

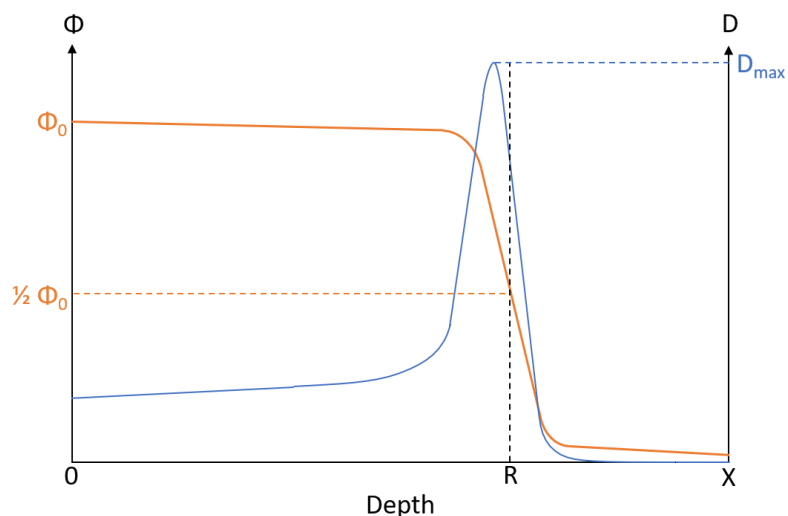


Figure 2.7. Plot of proton fluence (Φ) and dose (D) as a function of depth in a medium. 'R' denotes the average proton range. (Figure adapted from Lu⁴².)

The dose-depth plot of a single proton would have a very distinct Bragg peak, but a plot with many contributing protons has a broadened Bragg peak due to the variance in exact range and energy loss rate of each proton during its travel. This variation increases with penetration depth and, therefore, with proton energy, meaning that higher energy proton beams result in broader Bragg peaks⁵¹. The mean proton range, R , is defined as the depth where the fluence has been reduced to half of its original value. It should be noted that the depth R does not exactly align with the maximum dose depth. Rather, R generally occurs at a depth with 80-90% of the maximum dose deposition, D_{max} , on the falling edge of the dose-depth plot⁴². This distinction is important to keep in mind, as many proton range studies are performed using dose measurements rather than fluence measurements and the range must be determined accordingly.

2.4 Radiation Shielding Materials

In order to minimize the risk presented by the complex radiation environment in deep space, the three well-established principles for minimizing radiation exposure are applied: minimizing exposure time, maximizing distance between radiation sources and crew, and providing sufficient radiation shielding to workers^{56,57}. In more typical radiation exposure scenarios like nuclear power plants and nuclear medical facilities, this approach can be implemented by limiting work shifts, utilizing robotics, and wearing shielded personal protective equipment. However, in the case of deep space exploration, the exposure time is defined by the mission and, since particles from GCRs and SPEs permeate space, distance is not a tunable factor. This leaves shielding as the only variable method of mitigating radiation exposure risk.

Standard radiation shielding for low-earth orbit (LEO) structures such as the International Space Station (ISS) has consisted primarily of aluminum^{16,58,59}. Because of the attenuation of cosmic radiation by Earth's atmosphere and the Van Allen belts, aluminum is sufficient to shield from most of the remaining radiation^{36,45}. Additionally, aluminum is lightweight, inexpensive, readily available, and structurally strong enough, when alloyed or used with additional materials like Kevlar, to function as both a structural material and as a shielding material. This provides protection from radiation as well as debris the spacecraft may encounter in space⁵⁸. Multifunctionality is important to consider, as cost and weight are significant prohibitors of space missions and fulfilling two requirements with a single component is more efficient for both cost and weight.

Missions beyond LEO inherently forfeit the radiation attenuation provided by Earth's atmosphere and the Van Allen belts, meaning the radiation environment contains higher energy and higher atomic number particles, on average, than the radiation environment in LEO. A greater number of HZE particles impacting a shielding material will cause more fragmentation events than lower energy and atomic number particles interacting with same material, resulting in the production of more secondary particles. This is a major concern with the use of standard LEO shielding materials in deep space applications, as secondary particles can contribute significantly to dose. A proposed

solution is the use of hydrogen and/or high hydrogen content materials, like polymers, for space radiation shielding. Hydrogen nuclei consist of a single proton and neutron, making them unable to fragment into lighter nuclei and biasing the fragmentation process towards projectile fragmentation^{23,60}.

While polymers make significant improvements over aluminum alloys in terms of reducing secondary particle production, pure polymer shielding solutions generally have far worse mechanical and thermal properties. This makes pure polymers a poor choice as a multifunctional component that must also provide structural and thermal shielding. In order to maintain the shielding properties of polymers while improving structural and thermal properties, various polymer-based composites have been proposed. Many combinations of fillers and polymers have been studied^{16,20,23,61–65}, but most literature on multifunctional applications has focused on nanocomposites. Polymer-based nanocomposites have shown improved mechanical properties over their microcomposite counterparts, as shown in Figure 2.8. It's hypothesized that these size effects are due to either surface-to-volume ratio effects, increased dispersion homogeneity with decreasing particle size, or a combination of the two causes^{66,67}.

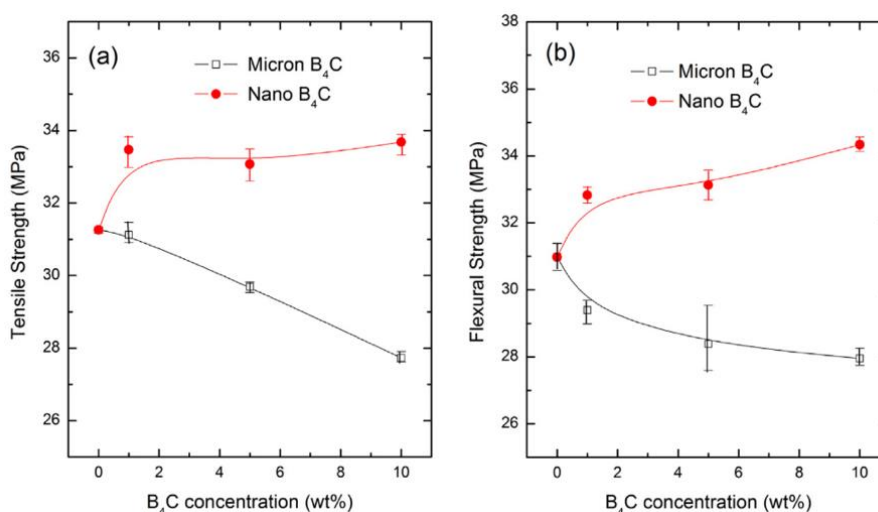


Figure 2.8. Plot of experimental results showing a) tensile strength and b) flexural strength as functions of B₄C filler concentration in a high-density polyethylene matrix for microscale and nanoscale filler particles. (Plots from Kim⁶⁷.)

Of the many proposed fillers for multifunctional nanocomposites, one of the most promising is carbon nanotubes. CNTs are of sheets of graphene which are rolled to create a tube whose wall is a single atomic layer of carbon. These novel nanostructures have become well-known for their incredibly high strength-to-weight ratio, with some experimentally measured elastic moduli nearing that of diamond¹⁷. Additionally, CNTs have high electrical and thermal conductivity and can be made to act metallic or semi-conductive based on the structure of the tube^{15,68}. Despite the seemingly simplistic nature of CNTs, the variety of ways a graphene sheet can be rolled into tubes necessitates a common descriptor to characterize the nanotube. A widely used characterization is the chiral vector,

$$\vec{C}_h = n\vec{a}_1 + m\vec{a}_2 \quad ,$$

where n and m are integers designating how many full lattice steps in each direction, \vec{a}_1 and \vec{a}_2 , span the circumference of the tube^{15,17}. Rather than specifying the chiral vector itself, the chirality of a nanotube is often described as (n, m) . Two special cases are the ‘armchair’ tubes, which occur when n and m are equal, and the ‘zigzag’ tubes, which occurs when m is equal to zero, both shown in Figure 2.9.

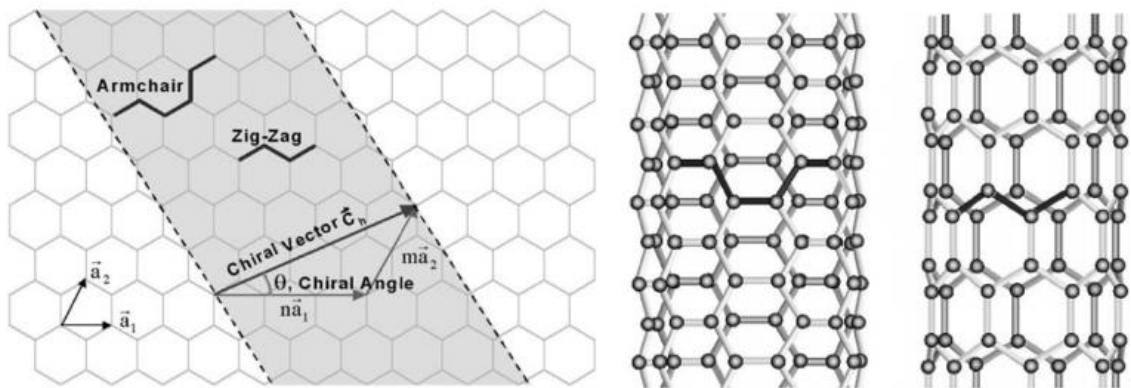


Figure 2.9. Diagram of nanotube characteristics as they relate to a sheet of graphene (left) and illustrations of armchair and zigzag nanotubes (right). (Figure from Thostenson¹⁷.)

2.5 Radiation Transport Modeling

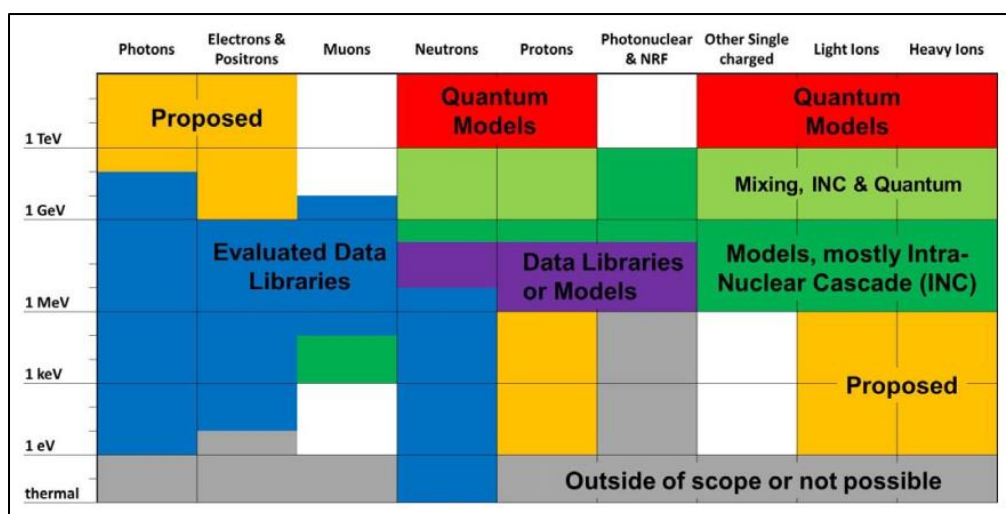
Advancements in computing technology and radiation transport physics models has resulted in increasingly advanced computational simulations of radiation transport scenarios. These models have progressed to address an extensive array of radiation environments, with applications in fields including nuclear energy, radiation shielding, nuclear nonproliferation, and medical physics. In order to simulate the fate and transport of radiation, many codes approximate the linear Boltzmann transport equation, which is an intricate mathematical description of particle interactions based on a variety of variables, including particle type, energy, density, fluence, and interaction cross section^{69,70}.

Because of the complex nature of the Boltzmann equation, it is difficult to solve analytically and is instead often approximated using mathematical and statistical techniques. Historically, there are four approaches used to approximate radiation transport using the Boltzmann equation: diffusion, discrete ordinates (S_N), spherical harmonics (P_N), and Monte Carlo⁷¹. The first three approximation methods are known as ‘deterministic’ methods, using various assumptions and discretization techniques to analytically approximate the Boltzmann transport equation for the system. In contrast, the Monte Carlo method simulates and tracks many individual particles, whose behavior is then used to estimate the average particle solution. While each approximation method has its merits in radiation transport, this study focuses on the Monte Carlo method.

One of the most well-known and broadly validated radiation transport codes is the Monte Carlo N-Particle (MCNP) code, a Fortran-based program developed and maintained by Oak Ridge National Laboratory. MCNP works by using a pseudo-random number generator to randomize particle characteristics within the bounds set by the user. The code then tracks each particle, using cross section data and physics models to determine interaction behavior between the particle and the medium it is traversing. This process is repeated until the particle either runs out of energy or is ‘lost,’ escaping the user-generated geometry. During the process, MCNP records specific user-requested values, like flux, energy deposition, and current, at points of interest and prints them to a

file for further analysis. Over the years, MCNP capabilities have expanded to include a large variety of particle types and energies. MCNP6 has merged the legacy code of two previous versions, MCNP5 and MCNPX, incorporating high-energy particles and light ions, as listed in Table 2.1.

Table 2.1. Table of the particle types and energies addressed in MCNP6 and their corresponding interaction physics. (Table from Goorley⁷².)



As discussed in Section 2.2, charged particles lose most of their energy by ionizing atoms as they traverse a material. The result is a large number of electrons that have been stripped from their original orbitals. Some of these knock-on electrons have enough kinetic energy after escaping to cause secondary ionization and are known as δ -rays. Until the latest version of MCNP, MCNP 6.2, simulated δ -ray production was limited to collisions where the incident particle was either an electron or a positron⁷³. For all other charged particles, the energy transferred from a charged particle to an electron was assumed to be deposited locally rather than producing delta radiation along a path. This is accounted for using the continuous slowing down approximation (CSDA), which assumes a charged particle continuously loses energy rather than losing energy in discrete

ionization events⁷⁴. However, the release of MCNP 6.2 introduced the inclusion of δ -ray production as a user-enabled feature for all energetic charged particles^{27,73}.

With advancements in MCNP radiation transport and the development of proton therapy over the past several decades, models analyzing high-energy protons and their interactions with certain mediums have been studied^{47,48,50,51}. However, the mediums studied have primarily been those most relevant to the medical use of proton beams: air, water, and tissue. By utilizing similar models, it is possible to study proton interactions with other mediums, though the computational limits on the scale and complexity of these mediums are still unknown.

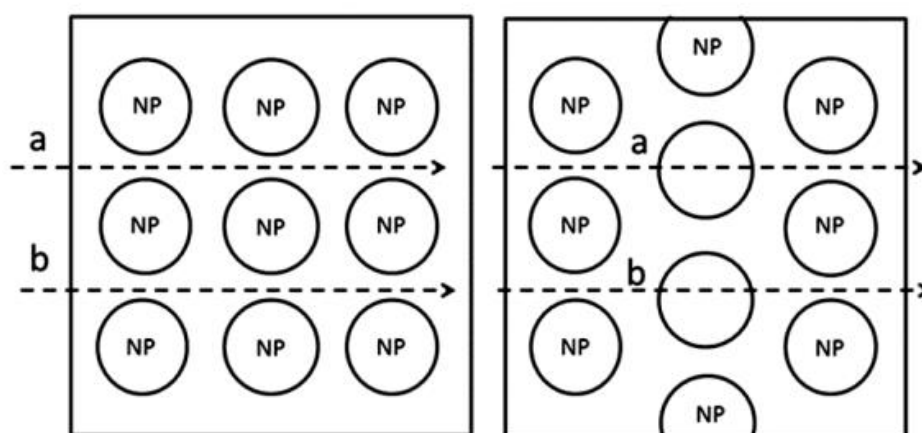


Figure 2.10. Schematics of nanoparticles (NP) in a simple cubic motif (left) and a staggered motif (right). (Image from Mansouri⁷⁵.)

Previous MCNP studies on nanocomposite radiation shielding have largely focused on applications involving gamma attenuation^{76–78} and neutron attenuation and detection^{67,75,79–81}. Additionally, literature on the topic have reported primarily on nanocomposites containing particle-type fillers rather than structured fillers, like nanotubes^{67,76,78,79,82}. Several publications describe the use of MCNP for studying polymer/nanotube composites, but do not specify the modeling technique used for the nanotubes^{77,83}. Mansouri, *et. al.*, (2020) theorized that disagreements between Monte

Carlo and experimental studies of nanocomposite containing particle-type fillers are due to inaccurately modeling particle locations. Most simulations model nanoparticles in a simple cubic motif (Figure 2.10, left) rather than a more complex motif (Figure 2.10, right) that more accurately represents the non-homogeneity of the true nanocomposite.

If Manouri's hypothesis is correct and inaccurate modeling of nanoscale materials does, in fact, affect the fidelity of radiation transport simulations, it may be true that the same is true for more complex nanostructures. The objective of this research is to investigate the modeling resolution necessary for Monte Carlo transport using MCNP6.2 to accurately predict the water equivalent thickness of shielding materials of interest for deep space exploration, including polymer-based nanocomposites. An experiment at the TRIUMF Proton Irradiation Facility is modeled in MCNP6.2 using three parameters – experimental setup geometry, particle tracking physics settings, and nanocomposite model geometry – in order to demonstrate the effect of these assumptions on MCNP's ability to reproduce measurements.

3 Methods

3.1 Li *et. al.* Experimental Data

3.1.1 Overview

Z. Li, *et. al.* (2013)¹⁶ outlines the performance of shielding materials including a polymer-based nanocomposite containing single-walled carbon nanotube (SWCNT) fillers in a high-energy proton beam. The study measures the stopping power and water equivalent thickness (WET) of several shielding materials. WET is a measurement used to compare the attenuation capabilities of different materials by measuring the thickness of water that is needed to attenuate an incident radiation beam to the same extent that the material of interest would attenuate the same beam. The concept of WET is shown in Figure 3.1, illustrating a particle beam of initial energy E_i traversing a medium m of thickness t_m . The particles escape the medium with an energy E_f and produce a range in water shown by the top right plot in Figure 3.1. The WET, t_w , is the thickness of box labeled 'Water,' which attenuates the same initial beam of energy E_i to the same final particle energy, E_f .

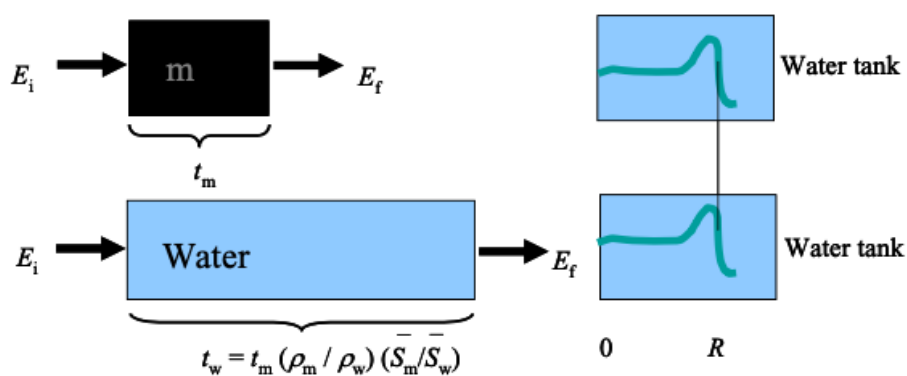


Figure 3.1. Schematic showing the concept of water equivalent thickness. (Figure from Newhauser⁵¹.)

The samples of interest were fabricated at the University of Waterloo and then irradiated in the BL2C proton beam at the TRIUMF Proton Irradiation Facility in Vancouver, Canada. A diagram of the BL2C proton beam experimental setup is shown in Figure 3.2, as published by Li, *et. al.* The components identified in the experimental setup are standard for proton and heavy ion therapy studies: the diagnostic ion chamber (DIC) and backup ion chamber (BIC), the range shifter, and the sample. The DIC and BIC are tools used to characterize the proton beam before and after passing through the range shifter and sample, respectively. The range shifter is a wedge of polymethyl methacrylate, also known as acrylic, whose thickness is adjusted by lowering or raising the shifter into the beamline, adjusting how much the beam is attenuated before reaching the sample.

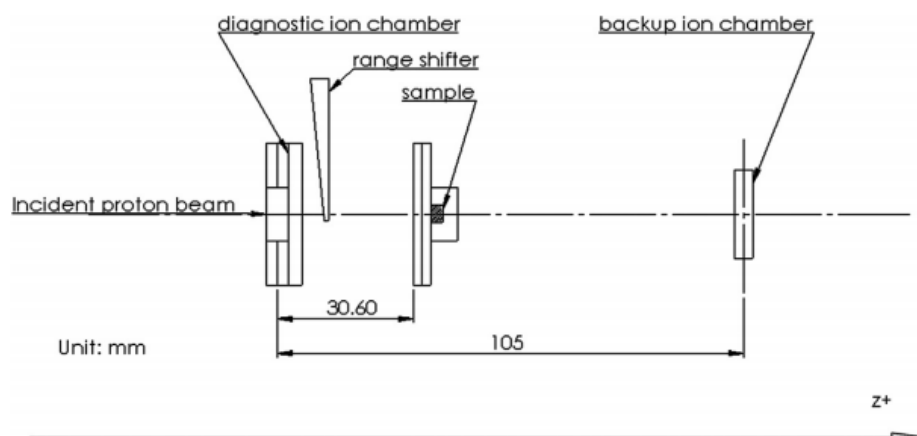


Figure 3.2. Simplistic diagram of the TRIUMF BL2C experimental setup used for proton irradiation testing. (Figure from Li¹⁶.)

In Li's study¹⁶, the range shifter thickness was incrementally increased in steps of 0.01 mm and the water equivalent doses measured by the DIC and BIC were recorded. Then, the BIC/DIC ratio was plotted as a function of range shifter thickness, revealing the Bragg peak, and the range shifter thickness at 90% of the maximum BIC/DIC ratio on the falling edge of the plot was recorded as $RS_{90\%}$, in units of 0.01 mm. For example, a

$RS_{90\%}$ value of 2450 corresponds to a range shifter thickness of 24.50 mm. The WET of the range shifter was then calculated using TRIUMF's calibration equation¹⁶:

$$t_{RS90\%}^{WET} = 1.156(2.23 + 1.0075 \times 10^{-2} \times RS_{90\%}) \quad .$$

The thickness of water needed to completely stop the proton beam of interest is approximately equal to sum of the sample WET and the range shifter WET. In order to calculate the WET of the samples, t^{WET} , the following relationship was used:

$$t^{WET} = t_E^{WET} - t_{RS90\%}^{WET} \quad ,$$

where t_E^{WET} is the stopping range of a proton beam of energy E in water, as calculated using the Stopping and Range of Ions in Matter (SRIM) software⁸⁴, and $t_{RS90\%}^{WET}$ is the WET of the range shifter for each experiment. This relationship fundamentally states that the thickness of water needed to stop a proton beam of energy E is equal to the sum of the WET of the sample and the WET of the range shifter at a thickness that corresponds to 90% of the maximum dose deposition.

3.1.2 Materials

The nanocomposite studied in Li's 2013 experiment was a polydimethylsiloxane (PDMS) polymer with 1.12 wt% SWCNTs dispersed in it. The SWCNTs had diameters of 1-2 nm and lengths of $\leq 30 \mu\text{m}$. Characterization of the nanotube dispersion and orientation Nanocomposite samples were tested separately in a 63 MeV and 105 MeV proton beam. Samples of aluminum and pure PDMS were also tested as standards for comparison. The performed experiments are outlined in Table 3.1 below. The beam was characterized to have a density of 2×10^8 protons/cm²/s and a beam diameter of 19 mm at the position of the sample. Each sample had cross section dimensions of 4 cm \times 4cm, with thicknesses listed in Table 3.1.

Table 3.1. Outline of each experiment performed, including beam energy, material, density, and sample thickness. (Table modified from Li¹⁶.)

Initial Beam Energy (MeV)	Material	Density (g/cm ³)	Sample Thickness (mm)
105	Aluminum	2.698	25.30
105	PDMS	1.033	48.65
105	PDMS/SWCNT	1.038	47.00
63	Aluminum	2.698	12.70
63	PDMS	1.033	24.10
63	PDMS/SWCNT	1.038	23.75

3.1.3 TRIUMF BL2C Setup

The experimental setup shown in the 2013 Li article shows only the components of the BL2C proton irradiation apparatus at the TRIUMF facility necessary to understand the WET results. However, a publication by Blackmore⁸⁵ shows a more details diagram of the irradiation equipment, as shown in Figure 3.3. While some of the equipment, like the components beyond the BIC, clearly have no effect on the measurements of interest in this study, other pieces of equipment may be important in replicating the physics, like the beam scatterer and collimators. Because the significance of these components is unclear, their presence must be considered in the computational model.

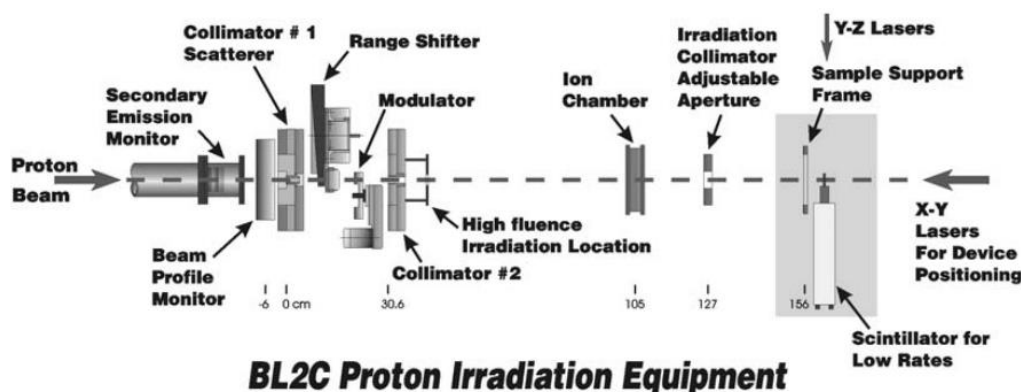


Figure 3.3. Complex diagram of the TRIUMF BL2C experimental setup used for proton irradiation testing. (Figure from Blackmore⁸⁵.)

3.2 MCNP Input

3.2.1 Experimental Setup Geometry

Using the experimental setup described in Li *et. al.*¹⁶ as well as the details provided by Blackmore⁸⁵ about the TRIUMF particle accelerator, two geometries were defined in MCNP, as shown below in Figure 3.4. The first geometry includes the proton beam source, DIC, RS, sample, and BIC, as described in Li, *et. al.* The second geometry includes all components of the first geometry as well as a beam scatterer and two collimators to more closely match the detailed TRIUMF design outlined by Blackmore^{85,86}. The first brass collimator consists of a 12 mm diameter aperture and, because the actual thickness of the lead scatterer was not specified for the experimental study, the scatterer thickness was approximated to be 0.01 mm. Published scatterer thicknesses and materials for experiments using the BL2C beam line vary drastically depending on the beam energy, range shifter thickness, and desired beam characteristics. Scatterers include 0 to 2.4 mm of lead or 0 to 0.3 mm of copper⁸⁷. The aperture of the second brass collimator is dependent on the patient when the beam is used for proton beam therapy, but was set to an aperture diameter of 19 mm for this study to match the spot size specified by Li^{16,86}. The collimator thickness was not specified, so the minimum thickness for the collimators was determined using SRIM⁸⁴, which calculates the range of ions traveling through a designated material. The SRIM output for hydrogen with an energy of 105 MeV, the maximum energy used in this study, in brass can be found in Appendix A.

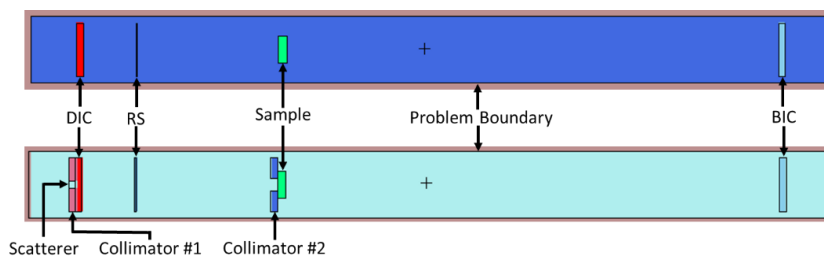


Figure 3.4. MCNP plot of the simplistic model (top) and complex model (bottom) of the experimental setup. Colors do not indicate characteristics of the cell.

A comparison of the MCNP output for two experimental setup geometries – one with the collimators and scatterer and one without – was done for an aluminum sample with an initial beam energy of 63 MeV and is discussed in the Results section. The complex geometry was used for all remaining radiation transport simulations. A difference that should be noted between the TRIUMF BL2C setup and the computation model is the value measured by the ion chambers; the ion chambers used in the physical experiments measure the water equivalent dose while this study computationally determined air equivalent dose in MCNP by setting the BIC and DIC materials to air. Because the experimental results are presented as a ratio of the BIC dose to DIC dose, the effect of the range shifter thickness on the beam modulation should not be affected by the ion chamber medium. In both geometries, the proton beam source was modeled as a disk source with a diameter of 12 mm, positioned 5 cm to the left of the scatterer and centered in the y - and z -directions. The initial beam energy was set to either 63 MeV or 105 MeV, depending on the experiment, to match the Li *et al.* experimental setup, and the source was oriented as a beam moving in the positive x -direction.

3.2.2 Physics Settings

Many computational proton therapy studies consider only protons and neutrons they tend to be the greatest contributors to patient dose^{88,89}. Secondary neutrons produced by nuclear interactions can be scattered to significant angles and can have drastically greater radiation weighting factors than some of the other particles produced, depending on neutron energy⁵⁴. Additionally, neutrons do not carry a charge and, therefore, do not undergo coulombic interactions, making them difficult to shield against. However, protons and neutrons are far from the only particles that exist in a proton therapy scenario. For example, electrons in the form of δ -rays are produced via ionization and heavier ions can be produced via target fragmentation.

The assumption that the contribution to dose from electrons and recoil ions is tested by simulating an aluminum sample in a 63 MeV proton beam using three distinct physics scenarios. In the first scenario, only protons and neutrons are tracked and δ -ray

production is turned off. In the second scenario, protons, neutrons, and electrons are tracked and δ -ray production is turned on using the default energy cutoff of 20 keV. In the third scenario, protons, neutrons, electrons, and light recoil ions (deuterons, tritons, helions, and alpha particles), and δ -ray production is turned on using the default energy cutoff of 20 keV. A comparison of the three scenarios against the experimental measurement is shown in the results section, along with the computational time for each.

3.2.3 Nanocomposite Geometry

Thermal, mechanical, and electrical properties of carbon nanotubes differ drastically from bulk carbon^{15,17,18}. Despite this distinction, no known studies have detailed the modeling of nanotube structures in codes like MCNP. In several studies referencing models of CNT nanocomposites, it is unclear which methods were used to develop the model and the level of detail it contains. To determine the effects of several common physics and geometry considerations on the fidelity of Monte Carlo radiation transport through nanoscale materials, three separate nanocomposite models were developed with varying levels of detail. Based on the sample size, CNT content, and CNT dimensions, the 2.375 cm-thick and 4.700 cm-thick nanocomposite samples tested by Li, *et. al.*, contain $\sim 10^{15}$ CNTs each. There are documented memory limitations with problems involving more than ~ 4 million voxels that prevent simulations of the full samples with a high level of detail^{90,91}. While studies have published that $\sim 10^{13}$ lattice points can be modeled so long as tallies are not considered in each lattice cell⁸², smaller samples (6.8E-5 cm x 6.8E-5 cm x 2.5E-5 cm) are modeled here to avoid memory limitations. The radius of the source disk is adjusted accordingly, and the rest of the modeled experiment remains unchanged. The MCNP input deck for the bulk method can be found in Appendix B.

The first approach models the nanocomposite sample as a single bulk material, assuming the carbon from the nanotubes becomes homogeneously dispersed with the hydrogen, oxygen, carbon, and silicon atoms of the PDMS. For a composite sample containing 1.12 wt% SWCNT in a PDMS matrix of chemical composition C_2H_6OSi , the

homogenous composite material was calculated to have a composition of 20.56 at% C, 59.58 at% H, 9.93 at% O, and 9.93 at% Si. A material in the MCNP input deck was assigned this composition and the sample cell was designated as this material.

The second approach models the nanocomposite as a PDMS matrix with monodirectional hollow carbon cylinders within it. To achieve this model, a single hollow cylinder with a wall thickness equal to the diameter of a single carbon atom, 140 pm, was modeled in a PDMS matrix and the MCNP lattice function was used to replicate the matrix in order to create the sample. Figure 3.5 shows an MCNP plot of the vertical cylinder geometry from the top and as a cross section of the cylinder.

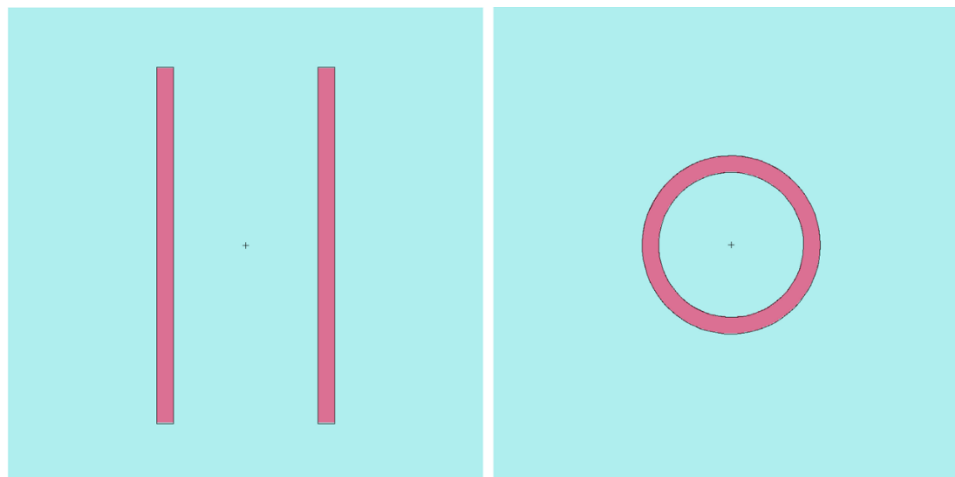


Figure 3.5. MCNP plot of a carbon nanotube cross section (left) and the top view of a single carbon nanotube (right) using the hollow cylinder nanotube method.

The third approach is a complex model of the nanocomposite as a PDMS matrix with carbon spheres representing each carbon atom in the nanotube. This model was developed by first modeling a carbon nanotube in the open source Nanotube Modeler software⁹², shown in Figure 3.6, which produces the three-dimensional Cartesian coordinates of the carbon atoms in the nanotube. The chirality of the nanotubes was estimated to be (18, 2) based on the diameter provided by Li, *et. al.* The Nanotube Modeler software, shown in Appendix C, lists the location of 544 carbon atoms constructing a single-walled nanotube with a length of 30 Å. This is significantly shorter

than the nanotubes used in the experimental testing but allows for MCNP radiation transport without encountering memory limitations. Figure 3.7 shows an MCNP plot of the atomistic nanotube geometry from the top and as a cross section of the nanotube structure.

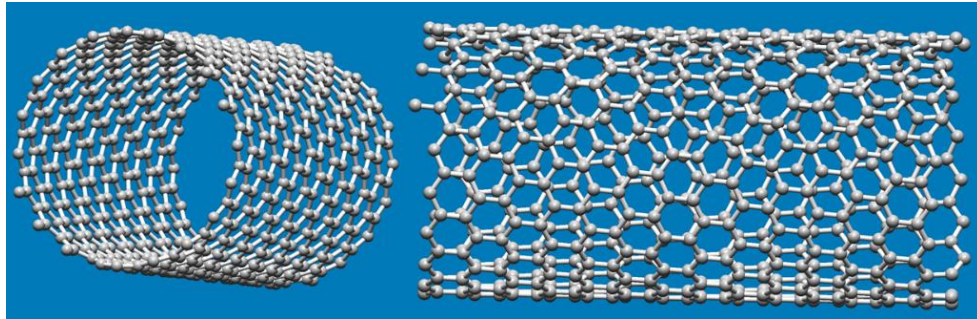


Figure 3.6. Angled view (left) and side view (right) of (18,2) nanotube in Nanotube Modeler software.

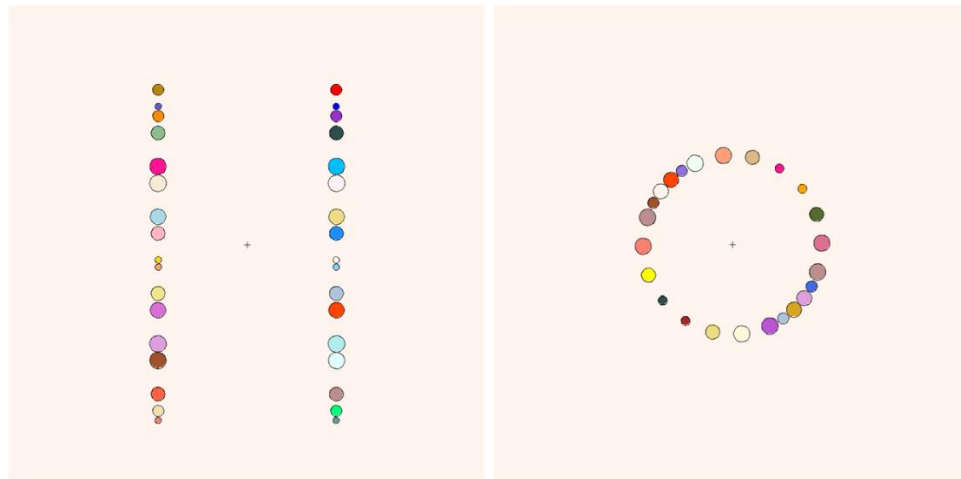


Figure 3.7. MCNP plot of a carbon nanotube cross section (left) and the top view of a single carbon nanotube (right) using the atomistic nanotube method.

Even with a high level of detail, it should be noted that there are several known inconsistencies between the models and the nanocomposites used in experiments that

may introduce some level of error. These differences include the aligned orientation and consistent length, diameter, and chirality of the modeled CNTs while the synthesized nanocomposite is assumed to have randomly oriented CNTs of varying length, diameter, and, possibly, chirality. The random nature of the CNT orientation in synthesized nanocomposites results in some of the CNTs overlapping and becoming ‘knotted’ with each other, which is not accounted for in the MCNP model. Additionally, the step size in range shifter thickness at TRIUMF is 0.01 mm but this study uses a step size of 0.20 mm in order to reduce overall computational time.

3.2.4 Tally Specification

Choosing a tally that is both useful in finding the information of interest and appropriate for the problem in question is central to producing meaningful results. For this reason, the approach outlined in a computational proton therapy study by Ryckman⁵⁰, which considers both protons and secondary neutrons, is applied. The F6 tally is used to monitor the energy deposition from protons and the F4 tally is used with the addition of a flux-to-dose conversion function to determine the dose contribution of secondary neutrons. The F6 and F4 tallies record the energy deposition and flux averaged over a cell, respectively.

Separate tallies are used for protons and neutrons due to the difference in the energy-dependence of their radiation weighting factors, which is a measure of the biological effectiveness of particular radiation type and energy⁹³. The radiation weighting factor of neutrons is highly energy-dependent, as shown in Figure 3.8, while protons are generally considered to have a single, energy-independent radiation weight factor, though there is some disagreement on this assumption⁵⁰. The F4 tally used to track the secondary neutrons is used in conjunction with a flux-to-dose conversion function from the NCRP-38 publication⁹⁴, which is included in the MCNP code. Since the proton radiation weighting factor is not energy-dependent, the F6 tally can be used without the need for a flux-to-dose conversion. A conversion factor of 1.602E-10 is applied to the proton tally to convert it from MeV/g to Gy and a radiation factor of 2 was applied in order to convert

absorbed proton dose to proton equivalent dose. Quality factors of electrons and ions are also considered energy-independent, so the F6 tally is also used in cases considering electrons and ions, with appropriate radiation weighting factors⁹⁴.

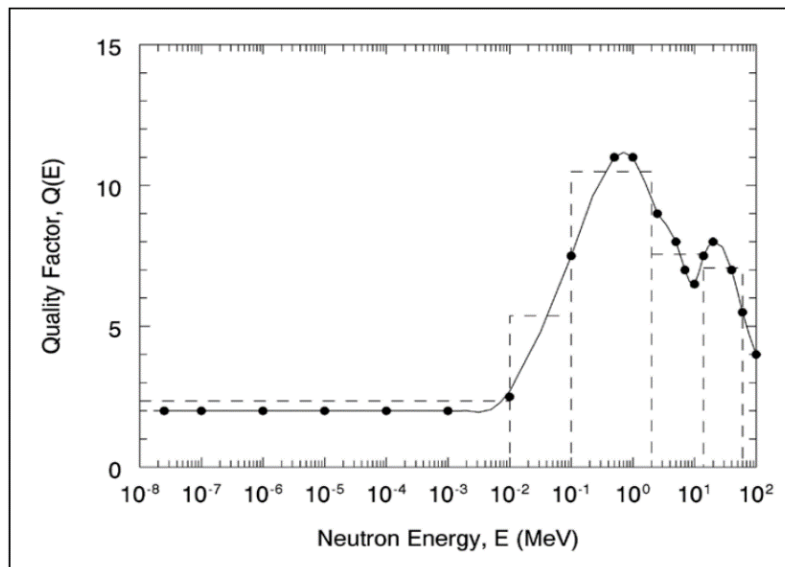


Figure 3.8. Plot of quality factor as a continuous function of neutron energy from NCRP Report 38 and a point-wise function described in ICRP Publication 60. (Plot from Kerr⁹⁵.)

3.3 Python Scripts

Because this study involves running a range of range shifter (RS) thicknesses, each of which require their own input file and MCNP run command, and create their own output files, extracting results for a single sample at a single energy can be very time-consuming. For a sample material, X , at a proton beam energy, E , with RS thicknesses ranging from A to B in steps of S , an input file would be manually created with a RS value of A and saved as *filenameA*. The input file would then have to be reopened, the RS value changed to $A+S$, and the file saved as *filenameA+S*. This would then be repeated until an RS value of B was reached. Once each of the input files were created, each would need to be run in MCNP individually. Then, the tally value and associated error would

have to be manually extracted from the output files and recorded in a separate file to plot. To create a more efficient, streamlined process for creating input files, running MCNP, and extracting data, several scripts were created using the Python programming language. A full record of each of the following scripts can be found in Appendix D.

3.3.1 Input File Generation

The first script, titled *expand.py*, was created to take an input file template, *filenameA*, with a given RS thickness, A , and replace the RS thickness with the next designated value, $A+S$, as well as save the changes to a new file, *filenameA+S*. Within this script, the user can designate a starting RS value, A , ending RS value, B , and the step size, S , as well as the file path for the template file, *filenameA*. Using this script, the user can create a single input file, for example *1800.txt* in a given folder, *C:/Users/Public/Desktop/Al_105MeV/*, and the script will generate the remaining files at the user-defined step size of range shifter thickness. Figure 3.9 below shows a folder before and after running the *expand.py* script, with a designated starting RS value of 1800, ending RS value of 2000, and step size of 50, as well as the surface cards of *1800.txt* and *1850.txt*, highlighting the difference between the two.

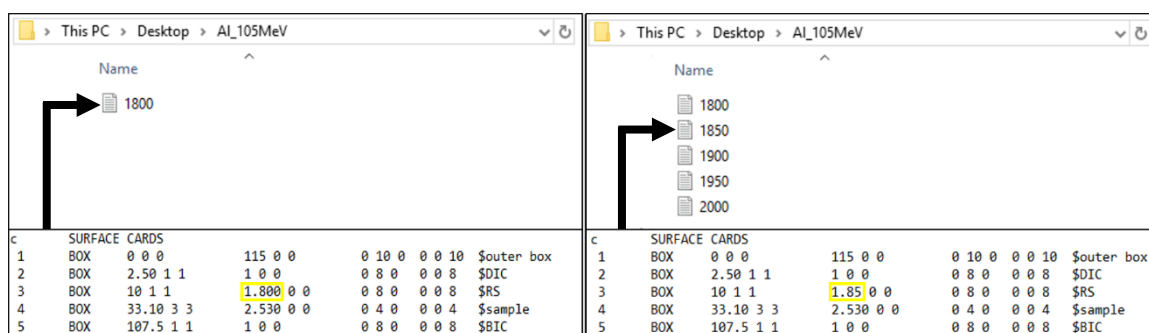
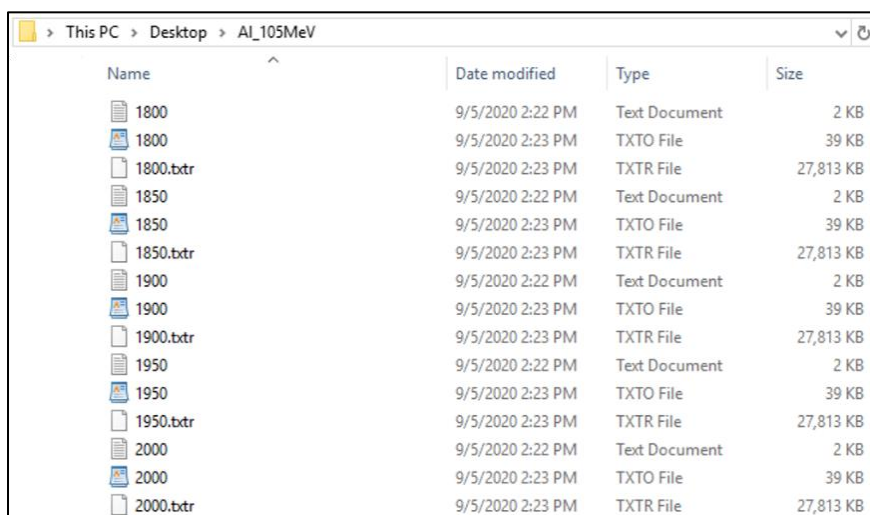


Figure 3.9. Image of a folder before (upper left) and after (upper right) running the *expand.py* script on it. The lower images show the change in range shifter thickness in the input files for manually generated *1800.txt* file (lower left) and automatically generated *1850.txt* file (lower right).

3.3.2 MCNP Run Command

The second script, `folder_run.py`, automatically enters the necessary command line “`mcnp62 N=filename`” – to run MCNP on each input file in a given folder. While this doesn’t reduce the actual computation time, it removes the need for the user to manually enter the run command for each file after confirming the previous run is complete. The `folder_run.py` code allows the user to designate, within the script, the file path of the folder containing the input files, run the Python program in a standard command terminal window, and periodically check on the progress. Figure 3.10 below shows a sample folder after running the `folder_run.py` script. Files designated “TXTO File” and “TXTR File” under the *Type* category are output files and run tape files, respectively, generated by MCNP.



Name	Date modified	Type	Size
1800	9/5/2020 2:22 PM	Text Document	2 KB
1800	9/5/2020 2:23 PM	TXTO File	39 KB
1800.bxtr	9/5/2020 2:23 PM	TXTR File	27,813 KB
1850	9/5/2020 2:22 PM	Text Document	2 KB
1850	9/5/2020 2:23 PM	TXTO File	39 KB
1850.bxtr	9/5/2020 2:23 PM	TXTR File	27,813 KB
1900	9/5/2020 2:22 PM	Text Document	2 KB
1900	9/5/2020 2:23 PM	TXTO File	39 KB
1900.bxtr	9/5/2020 2:23 PM	TXTR File	27,813 KB
1950	9/5/2020 2:22 PM	Text Document	2 KB
1950	9/5/2020 2:23 PM	TXTO File	39 KB
1950.bxtr	9/5/2020 2:23 PM	TXTR File	27,813 KB
2000	9/5/2020 2:22 PM	Text Document	2 KB
2000	9/5/2020 2:23 PM	TXTO File	39 KB
2000.bxtr	9/5/2020 2:23 PM	TXTR File	27,813 KB

Figure 3.10. Image of the folder after the `folder_run.py` script was used to run each input file through MCNP6.

3.3.3 Data Extraction

The third script, `extract.py`, extracts the tally values and errors from each output file within a designated folder of interest and prints the values to a comma separated

values (.csv) file, which can be opened in a variety of accessible programs, including Microsoft Excel and a broad range of text editors. Data extraction is done by searching each output file, line by line, for the cell title, which is printed just before the tally value and relative error in each tally table. The extracted tally values and errors are then put in lists as each file is searched and the lists are written to a new file, whose name can be designated within the script. For this study, the extracted data included range shifter thickness (*RS*), proton tally values within the DIC and BIC, the relative errors associated with the proton tallies, the neutron tally values within the DIC and BIC, and the relative errors associated with the neutron tallies. The data extraction script also searches the table of statistical checks implemented by MCNP for each tally, printing 'yes' if all the checks are met and 'no' if one or more of the checks are not met.

4 Results & Discussion

4.1 Experimental Setup Results

Radiation transport of proton irradiation using the simplistic and complex experimental setups were simulated using MCNP6.2 for an aluminum sample in a 63 MeV proton beam with range shifter thicknesses from 2 mm to 10 mm. The ratio of total dose within the BIC and the DIC are plotted as a function of range shifter thickness, as shown in Figure 4.1 below. It appears that removing the scatterer and collimators increased the magnitude of the peak but had no significant effect on the shape or spread of the Bragg peak. Since the average proton range is determined by the shape and position of the Bragg peak, it is also not substantially different between the two experimental setups. Error bars are included in all plots but are smaller than the data point markers for a majority of the data.

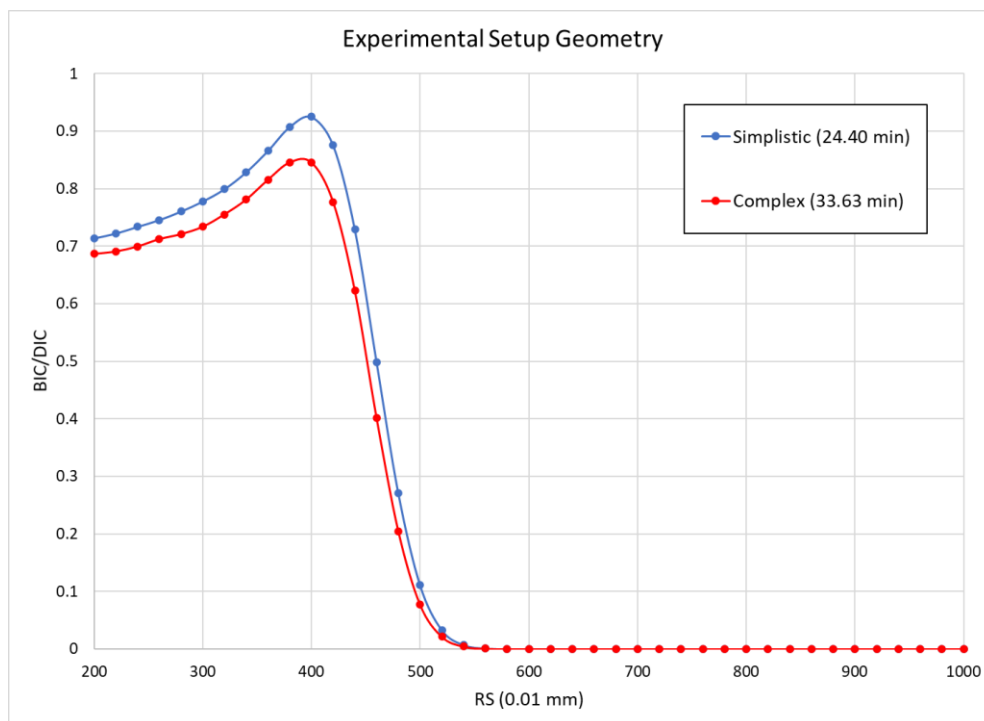


Figure 4.1. Comparison of BIC/DIC results for MCNP simulations of an aluminum sample in a 63 MeV proton beam with a simplistic and complex experimental setup geometry.

4.2 Physics Parameter Results

Radiation transport for an aluminum sample in a 63 MeV proton beam was simulated in MCNP6.2 for range shifter thicknesses ranging from 2 mm to 10 mm under three different physics settings. The first test, labeled ‘ $h + n$ ’ in Figure 4.2, considered only protons and neutrons, ignoring δ electrons and any ions that may have been produced or perturbed from rest during irradiation. The second test, labeled ‘ $h + n + \delta$,’ considered protons and neutrons as well as δ electrons, but ignored recoil ions. The third test, labeled ‘ $h + n + \delta + ions$ ’ in Figure 4.2, considered protons, neutrons, δ electrons, and light ions from proton elastic scattering events within the medium. The values following the labels in the plot legend indicate the computational time in minutes for a range shifter thickness of 6 mm (RS = 600) with the corresponding physics settings.

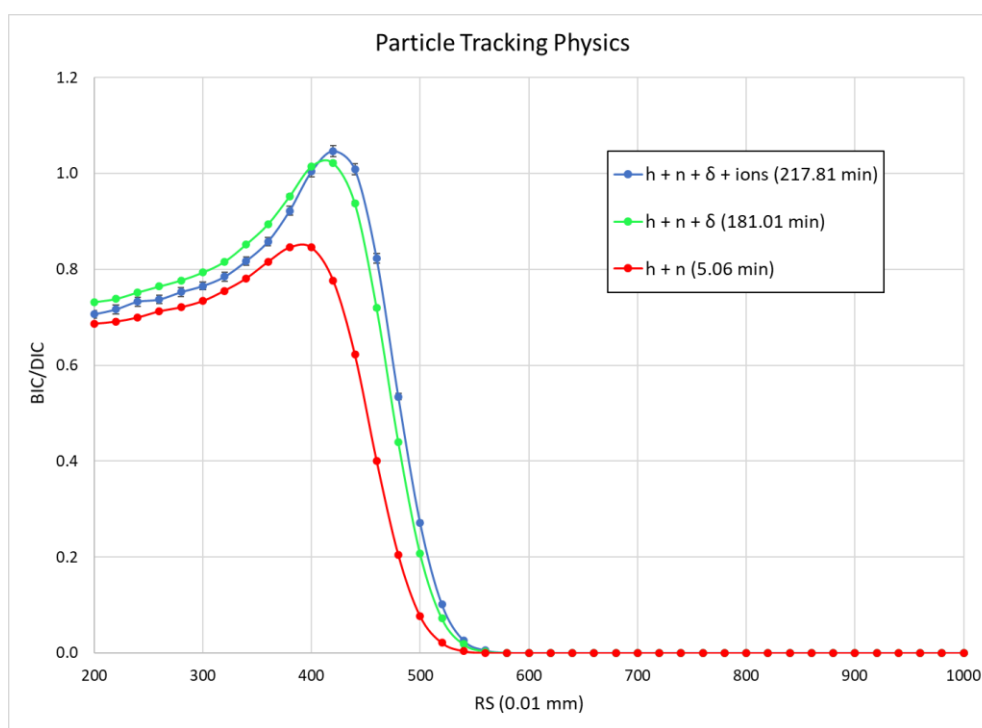


Figure 4.2. Comparison of BIC/DIC results for three different MCNP simulations of an aluminum sample in 63 MeV proton beam, each with different physics settings.

The addition of δ -ray tracking results in a large increase in the BIC/DIC ratio, indicating that, even with a radiation weighting factor of 1, δ electrons contribute significantly to the BIC equivalent dose. However, δ -ray tracking also increases the computational time by a factor of 8, which may be a limitation in large-scale, complex studies. Adding light ion recoil slightly increased the magnitude of the Bragg peak and shifted it further to the right. It also increased the computational time, but not to the same extent as the δ -ray tracking. The BIC/DIC ratio reached a maximum value of greater than 1 in several tests, which does not make physical sense, considering the experimental results showed substantial attenuation of the proton beam via the range shifter and the sample shielding material. This discrepancy may be due to model inaccuracies regarding the scatterer composition and thickness.

4.3 Nanocomposite Geometry Results

The nanocomposite sample was modeled in three different ways: 1) as a bulk, homogenous mixture of PDMS (hydrogen, oxygen, carbon, and silicon) and carbon from the CNTs, 2) as a PDMS medium containing vertically oriented, evenly spaced hollow cylinders of carbon, and 3) as PDMS with spherical carbon atoms suspended within it to produce nanotube structures. Radiation transport for each composite geometry was simulated using the complex experimental setup and tracking only protons and neutrons for range shifter thicknesses of 20 mm to 30 mm, shown in Figure 4.3. Increasing model resolution of the nanocomposite seems to have no discernable effect on radiation transport. The Bragg peak is nearly identical in both magnitude and shape for all three modeling methods, with a maximum BIC/DIC ratio difference of <1% between the models. Computational times did not vary much between the methods, either, as denoted in the legend.

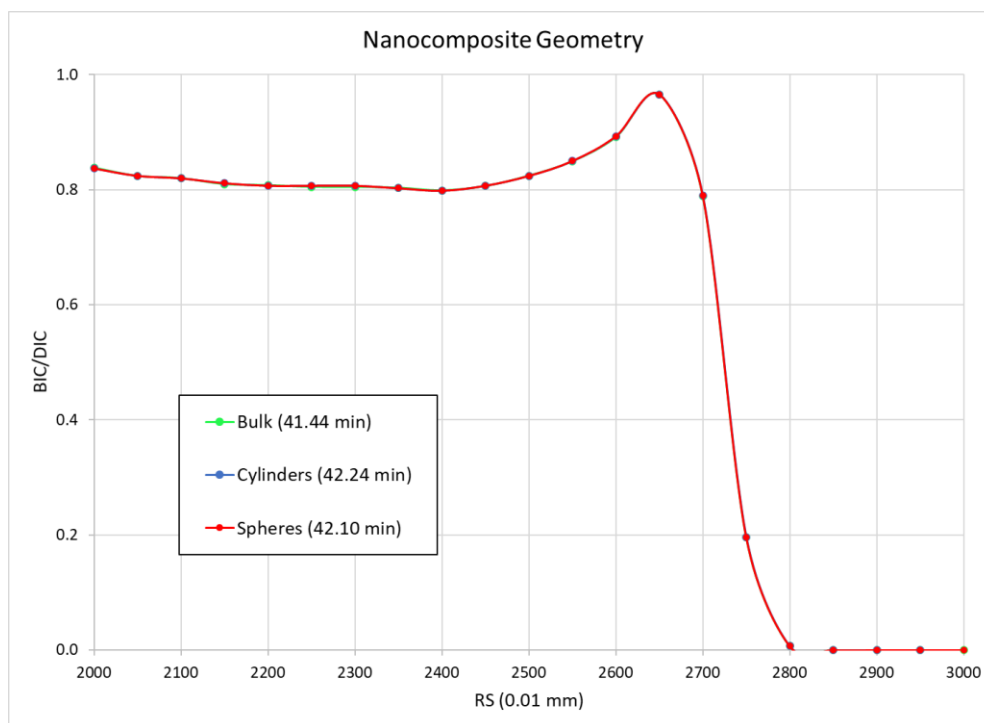


Figure 4.3. Comparison of BIC/DIC results for MCNP simulations of three nanocomposite models, tracking only protons and neutrons. Times in legend indicate computational time for a single run with a range shifter thickness of 26 mm.

4.4 Experimental Comparison

Comparing radiation transport results for aluminum, PDMS, and bulk nanocomposite with the experimental results published by Li, *et. al.*, in Figure 4.4, there are clear similarities and differences. The magnitude of the computational results differs considerably from the experimental results. This is likely due to the known differences between the modeled experimental setup and the actual setup. A relatively small difference in the scatterer composition or thickness can vastly alter the proton beam profile⁸⁷. As far as the shape and relative position, the computational results follow the same trends as the experimental results. The difference in the computational and experimental results is quantified in Table 4.1, which lists the WET values and the computed/experimental (C/E) ratio calculated from each set of results. It should be noted that the range shifter step size was 0.01 mm in Li's publication¹⁶ and 0.20 mm in this

computational study. The trend in C/E values suggest that the accuracy of the modeling methods discussed in this work may be energy dependent, with $C/E > 1$ for all 63 MeV tests and $C/E < 1$ for all 105 MeV tests. However, comparisons would need to be made at many more energies in order to draw conclusions on energy dependence of modeling accuracy.

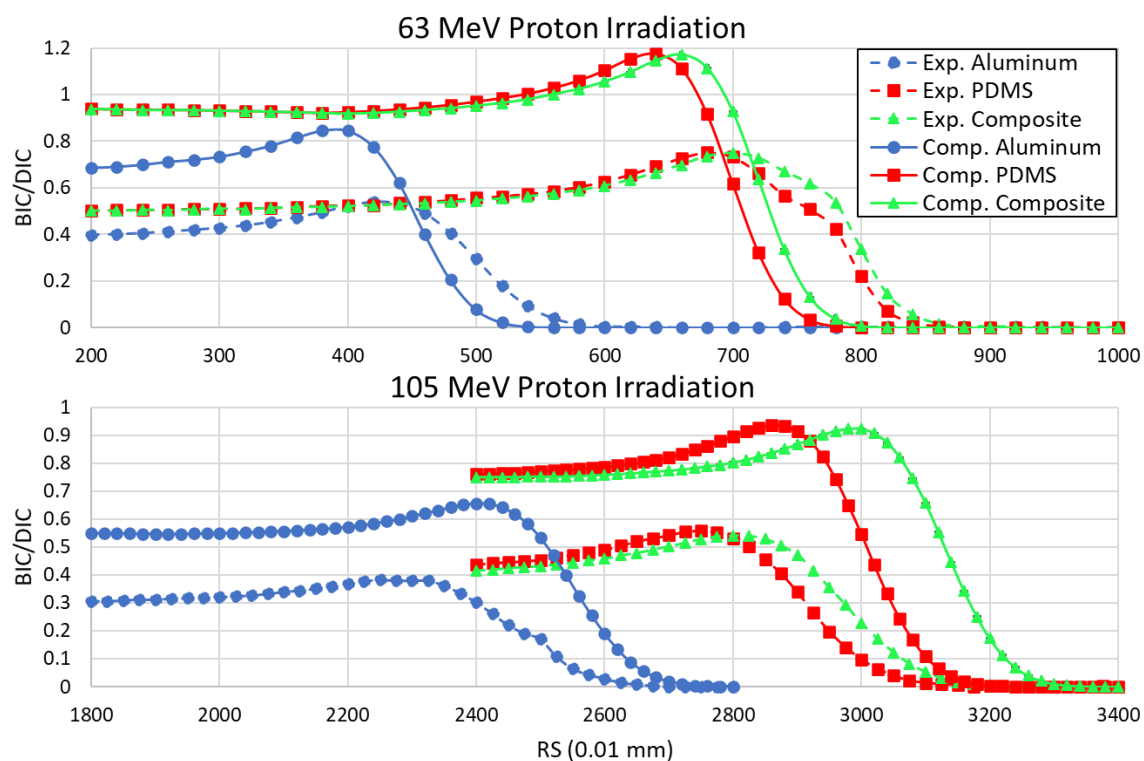


Figure 4.4. Experimental (dotted) and computational (solid) results of proton irradiation at 63 MeV and 105 MeV. Experimental data from Li^{16} .

Table 4.1. Experimental and MCNP results for each sample at each initial beam energy. *Experimental results from Li¹⁶.

WET Result Comparison					
Sample & Initial Beam Energy	Experimental* RS_{90%}	MCNP RS_{90%}	Experimental* WET (mm)	MCNP WET (mm)	Computed/Experimental Ratio
Aluminum, 105 MeV	2368	2480	52.77	51.46	0.9752
PDMS, 105 MeV	2844	2930	47.22	46.22	0.9788
PDMS/CNT, 105 MeV	2889	3060	46.70	44.70	0.9572
Aluminum, 63 MeV	462	420	25.26	25.75	1.019
PDMS, 63 MeV	717	670	22.30	22.84	1.024
PDMS/CNT, 63 MeV	738	690	22.05	22.61	1.025

5 Conclusion

Various geometry and physics parameters were altered in MCNP models and the radiation transport results were compared to experimental results in order to determine how the parameters affect the accuracy of the simulations. The results of this study indicate that the physics settings implemented in MCNP have the greatest influence on radiation transport out of the three variables that were considered. MCNP6.2's δ -ray production capabilities may prove to be an important addition if interested in quantifying dose, but the significant increase in computational time should be considered before implementation. The effect of the accuracy of experimental setup geometry on radiation transport depends largely on the component in question and the quantity of interest. For example, excluding the scatterer and collimators had little effect on the resulting proton range, but did increase the magnitude of the BIC/DIC dose ratio, indicating that it does affect the dose to each ion chamber. The scatterer composition and thickness are known to have a large influence on the proton beam profile and may contribute to the deviation between the experimental and computational results in this work.

Finally, the model resolution of the nanocomposite itself has no discernable influence on the simulated proton range or computational time, demonstrating a maximum difference of less than 1% in the BIC/DIC dose ratios of the three models for a single range shifter thickness. This result is encouraging for the argument of using radiation transport as a method of decreasing materials development lead time for nanocomposite shielding, as the input decks for bulk nanocomposites are far simpler than for atomistic representations of nanocomposites and, as shown in this study, produce identical results. Further supporting this conclusion, the computed WET for the PDMS/CNT nanocomposite agreed well with experimental values despite the known discrepancies in scatterer characteristics, with a C/E ratio of 1.025 in a 63 MeV proton beam and 0.9572 in a 105 MeV proton beam. It should be noted that this study looks only at high-energy protons fields and that these conclusions may not extend to other types of radiation or for different radiation energy ranges.

The results of this study provide foundational knowledge for future radiation transport studies of nanoscale materials in high-energy charged particle fields. Future work includes testing further physics assumptions, like the default exclusion of Cerenkov photons and a comparison of Vavilov models and CSDA models of charged particle straggling. Additionally, radiation transport of nanocomposite materials could be done using complex source descriptions that more accurately represent the expected radiation environment. Further comparisons of computational and experimental work at various energy levels may provide insight on possible correlations between charged particle energy and simulation accuracy.

Bibliography

1. Mars One will settle men on mars in 2023. Mars One. <https://www.mars-one.com/news/press-releases/mars-one-will-settle-men-on-mars-in-2023>. Accessed October 25, 2020.
2. Linck E, Crane KW, Zuckerman BL, et al. *Evaluation of a Human Mission to Mars by 2033*. IDA Science and Technology Policy Institute; 2019.
3. Wall M. 50 Years After Apollo 11, a Mars Landing is the Next Giant Leap, NASA Chief Says. Space. <https://www.space.com/nasa-mars-landing-apollo-11-50th-anniversary.html>. Published 2019. Accessed October 25, 2020.
4. Cucinotta FA, Hu S, Schwadron NA, Kozarev K, Townsend LW, Kim MY. Space radiation risk limits and Earth-Moon-Mars environmental models. *Sp Weather*. 2010;8(12).
5. Wilson JW, Anderson BM, Cucinotta FA, Ware J, Zeitlin CJ. Spacesuit Radiation Shield Design Methods. In: *SAE Technical Paper Series*. ; 2010. doi:10.4271/2006-01-2110
6. Saganti PB, Cucinotta FA, Wilson JW, Simonsen LC, Zeitlin C. Radiation climate map for analyzing risks to astronauts on the Mars surface from galactic cosmic rays. In: *2001 Mars Odyssey*. Springer; 2004:143-156.
7. Durante M. Biomarkers of space radiation risk. *Radiat Res*. 2005;164(4):467-473.
8. Durante M. Space radiation protection: Destination Mars. *Life Sci Sp Res*. 2014. doi:10.1016/j.lssr.2014.01.002
9. Cucinotta FA, Durante M. Risk of radiation carcinogenesis. *Hum Heal Perform risks Sp Explor Mission NASA SP-2009-3405 Houst Natl Aeronaut Sp Adm*. 2009:119-170.
10. Durante M, Cucinotta FA. Heavy ion carcinogenesis and human space exploration. *Nat Rev Cancer*. 2008;8(6):465-472.
11. National Research Council. *Technology for Small Spacecraft*. National Academies Press; 1994.
12. Moser T, Miller G. Structural Design - Orbiter Structural Design. *Eng Innov*.;273-275.
13. Townsend LW. Implications of the space radiation environment for human exploration in deep space. *Radiat Prot Dosimetry*. 2005;115(1-4):44-50.
14. Structures, Materials and Mechanisms. NASA. <https://www.nasa.gov/smallsat-institute/sst-soa/structures-materials-and-mechanisms>. Accessed October 25, 2020.
15. Dresselhaus MS, Dresselhaus G, Saito R. Physics of carbon nanotubes. *Carbon N Y*. 1995;33(7):883-891.
16. Li Z, Nambiar S, Zheng W, Yeow JTW. PDMS/single-walled carbon nanotube composite for proton radiation shielding in space applications. *Mater Lett*.

- 2013;108:79-83.
17. Thostenson ET, Ren Z, Chou T-W. Advances in the science and technology of carbon nanotubes and their composites: a review. *Compos Sci Technol*. 2001;61(13):1899-1912.
 18. Moniruzzaman M, Winey KI. Polymer nanocomposites containing carbon nanotubes. *Macromolecules*. 2006;39(16):5194-5205.
 19. Takakura A, Beppu K, Nishihara T, et al. Strength of carbon nanotubes depends on their chemical structures. *Nat Commun*. 2019;10(1):1-7.
 20. Li Q, Wei Q, Zheng W, et al. Enhanced radiation shielding with conformal light-weight nanoparticle–polymer composite. *ACS Appl Mater Interfaces*. 2018;10(41):35510-35515.
 21. Li Z, Chen S, Nambiar S, et al. PMMA/MWCNT nanocomposite for proton radiation shielding applications. *Nanotechnology*. 2016;27(23):234001.
 22. Borjanović V, Bistričić L, Mikac L, et al. Polymer nanocomposites with improved resistance to ionizing radiation. *J Vac Sci Technol B, Nanotechnol Microelectron Mater Process Meas Phenom*. 2012;30(4):41803.
 23. Harrison C, Weaver S, Bertelsen C, Burgett E, Hertel N, Grulke E. Polyethylene/boron nitride composites for space radiation shielding. *J Appl Polym Sci*. 2008;109(4):2529-2538.
 24. Holzer BJ. Introduction to particle accelerators and their limitations. *arXiv Prepr arXiv170509601*. 2017.
 25. Barbalat O. *Applications of Particle Accelerators*. CERN; 1994.
 26. Silari M. Applications of particle accelerators in medicine. *Radiat Prot Dosimetry*. 2011;146(4):440-450.
 27. Werner CJ. *MCNP User's Manual-Code Version 6.2*. Los Alamos, NM: Los Alamos National Laboratory; 2017.
 28. Mars & Beyond: The Road to Making Humanity Multiplanetary. SpaceX. <https://www.spacex.com/human-spaceflight/mars/>. Accessed January 20, 2021.
 29. Roadmap. Mars One. <https://www.mars-one.com/mission/roadmap>. Accessed January 20, 2021.
 30. Dunbar B. Moon to Mars Overview. National Aeronautics and Space Administration. <https://www.nasa.gov/topics/moon-to-mars/overview>. Published 2020. Accessed January 20, 2021.
 31. Early Bird, or Intelsat I. Encyclopædia Britannica.
 32. Lebel EA, Rusek A, Sivertz MB, Yip K, Thompson KH, Tafrov ST. Analyses of the secondary particle radiation and the DNA damage it causes to human keratinocytes. *J Radiat Res*. 2011;52(6):685-693.
 33. Cucinotta FA, Durante M. Cancer risk from exposure to galactic cosmic rays:

- implications for space exploration by human beings. *Lancet Oncol.* 2006;7(5):431-435.
34. Simpson JA. Elemental and isotopic composition of the galactic cosmic rays. *Annu Rev Nucl Part Sci.* 1983;33(1):323-382.
 35. Adams JH, Hathaway DH, Grugel RN, et al. *Revolutionary Concepts of Radiation Shielding for Human Exploration of Space.*; 2005.
 36. Benton ER, Benton E V. Space radiation dosimetry in low-Earth orbit and beyond. *Nucl Instruments Methods Phys Res Sect B Beam Interact with Mater Atoms.* 2001. doi:10.1016/S0168-583X(01)00748-0
 37. Guo J, Zeitlin C, Wimmer-Schweingruber RF, et al. MSL-RAD radiation environment measurements. *Radiat Prot Dosimetry.* 2015;166(1-4):290-294.
 38. Gleber M. CME Week: The Difference Between Flares and CMEs. National Aeronautics and Space Administration.
 39. What is Space Radiation? National Aeronautics and Space Administration, Johnson Space Center. <https://srag.jsc.nasa.gov/spaceradiation/what/what.cfm>. Published 2019. Accessed March 24, 2020.
 40. Rask J, Vercoutere W, Krause A, Navarro B. *Space Faring: The Radiation Challenge.* Huntsville, AL; 2008. https://www.nasa.gov/pdf/284275main_Radiation_HS_Mod3.pdf.
 41. Saganti PB. MARIE measurements and model predictions of solar modulation of galactic cosmic rays at Mars. 2005.
 42. Lu H-M, Flanz J, Paganetti H. *Physics of Particle Beams.* 2014.
 43. Zeitlin C, La Tessa C. The role of nuclear fragmentation in particle therapy and space radiation protection. *Front Oncol.* 2016;6:65.
 44. Trovati S, Ballarini F, Battistoni G, et al. Human exposure to space radiation: role of primary and secondary particles. *Radiat Prot Dosimetry.* 2006;122(1-4):362-366.
 45. Howell E. Van Allen Radiation Belts: Facts & Findings. Space. <https://www.space.com/33948-van-allen-radiation-belts.html>. Published 2018. Accessed March 24, 2020.
 46. Simonsen LC, Zeitlin C. Briefing to NAC HEO/SMD joint committee meeting Mars radiation environment—What have we learned. 2017.
 47. Paganetti H. *Proton Beam Therapy.* IOP Publishing Bristol; 2017.
 48. Li Z, Slopsma R. *Beam Delivery Techniques: Passive Scattering Proton Beams.* 2010.
 49. Wouters BG, Lam GKY, Oelfke U, Gardey K, Durand RE, Skarsgard LD. Measurements of relative biological effectiveness of the 70 MeV proton beam at TRIUMF using Chinese hamster V79 cells and the high-precision cell sorter assay.

- Radiat Res.* 1996;146(2):159-170.
50. Ryckman JM. Using MCNPX to calculate primary and secondary dose in proton therapy. 2011.
 51. Newhauser WD, Zhang R. The physics of proton therapy. *Phys Med Biol.* 2015;60(8):R155.
 52. Wisenbaugh ES, Andrews PE, Ferrigni RG, et al. Proton beam therapy for localized prostate cancer 101: basics, controversies, and facts. *Rev Urol.* 2014;16(2):67.
 53. De Los Santos J, Popple R, Agazaryan N, et al. Image guided radiation therapy (IGRT) technologies for radiation therapy localization and delivery. *Int J Radiat Oncol Biol Phys.* 2013;87(1):33-45.
 54. Park SH, Kang JO. Basics of particle therapy I: physics. *Radiat Oncol J.* 2011;29(3):135.
 55. Martin JE. *Physics for Radiation Protection.*; 2000.
 56. Protecting Yourself from Radiation. United State Environmental Protection Agency. <https://www.epa.gov/radiation/protecting-yourself-radiation#timedistanceshielding>. Accessed September 23, 2020.
 57. Kim JH. Three principles for radiation safety: time, distance, and shielding. *Korean J Pain.* 2018;31(3):145.
 58. Barry PL. Home, Space Home. NASA Science. https://science.nasa.gov/science-news/science-at-nasa/2001/ast14mar_1. Published 2001. Accessed September 23, 2020.
 59. Thibeault SA, Fay CC, Lowther SE, et al. Radiation Shielding Materials Containing Hydrogen, Boron, and Nitrogen: Systematic Computational and Experimental Study. Phase I. 2012.
 60. Norbury JW, Miller J, Adamczyk AM, et al. Nuclear data for space radiation. *Radiat Meas.* 2012;47(5):315-363.
 61. Beyerlein IJ, Caro A, Demkowicz MJ, Mara NA, Misra A, Uberuaga BP. Radiation damage tolerant nanomaterials. *Mater Today.* 2013. doi:10.1016/j.mattod.2013.10.019
 62. Cucinotta FA, Kim MHY, Ren L. Evaluating shielding effectiveness for reducing space radiation cancer risks. *Radiat Meas.* 2006. doi:10.1016/j.radmeas.2006.03.011
 63. Demkowicz MJ, Bellon P, Wirth BD. Atomic-scale design of radiation-tolerant nanocomposites. *MRS Bull.* 2010;35(12):992-998. doi:10.1557/mrs2010.704
 64. Mani V, Prasad NS, Kelkar A. Ultra high molecular weight polyethylene (UHMWPE) fiber epoxy composite hybridized with Gadolinium and Boron nanoparticles for radiation shielding. In: *Planetary Defense and Space Environment Applications.* Vol 9981. International Society for Optics and

- Photonics; 2016:99810D.
65. Nambiar S, Yeow JTW. Polymer-composite materials for radiation protection. *ACS Appl Mater Interfaces*. 2012. doi:10.1021/am300783d
 66. Schrempp-Koops L. SIZE EFFECTS ON THE EFFICIENCY OF NEUTRON SHIELDING IN NANOCOMPOSITES—A FULL-RANGE ANALYSIS. *Int J Nanosci*. 2013;12(03):1350015.
 67. Kim J, Lee B-C, Uhm YR, Miller WH. Enhancement of thermal neutron attenuation of nano-B₄C,-BN dispersed neutron shielding polymer nanocomposites. *J Nucl Mater*. 2014;453(1-3):48-53.
 68. Winey KI, Kashiwagi T, Mu M. Improving electrical conductivity and thermal properties of polymers by the addition of carbon nanotubes as fillers. *Mrs Bull*. 2007;32(4):348-353.
 69. *Attila User's Manual*. Gig Harbor, WA: Varex Imaging; 2019.
 70. Rose C. Comparison of Attila SN Particle Transport Code with MCNP in the Analysis of Small Modular Reactor Shielding. 2020.
 71. Brunner TA. Forms of approximate radiation transport. *Sandia Rep*. 2002.
 72. Goorley JT, James MR, Booth TE, et al. *Initial MCNP6 Release Overview-MCNP6 Version 1.0*. Los Alamos National Lab.(LANL), Los Alamos, NM (United States); 2013.
 73. Anderson C, McKinney G, Tutt J, James M. Delta-ray Production in MCNP 6.2. 0. *Phys Procedia*. 2017;90:229-236.
 74. Zieb K, Hughes HG, James MR, Xu XG. Review of heavy charged particle transport in MCNP6. 2. *Nucl Instruments Methods Phys Res Sect A Accel Spectrometers, Detect Assoc Equip*. 2018;886:77-87.
 75. Mansouri E, Mesbahi A, Malekzadeh R, Janghjoo AG, Okutan M. A review on neutron shielding performance of nanocomposite materials. *Int J Radiat Res*. 2020;18(4):611-622.
 76. Alavian H, Tavakoli-Anbaran H. Study on gamma shielding polymer composites reinforced with different sizes and proportions of tungsten particles using MCNP code. *Prog Nucl Energy*. 2019;115:91-98.
 77. El-Soad AMA, Sayyed MI, Mahmoud KA, Şakar E, Kovaleva EG. Simulation studies for gamma ray shielding properties of Halloysite nanotubes using MCNP-5 code. *Appl Radiat Isot*. 2019;154:108882.
 78. Kim J, Seo D, Lee BC, Seo YS, Miller WH. Nano-W Dispersed Gamma Radiation Shielding Materials. *Adv Eng Mater*. 2014;16(9):1083-1089.
 79. Mortazavi SMJ, Kardan M, Sina S, Baharvand H, Sharafi N. Design and fabrication of high density borated polyethylene nanocomposites as a neutron shield. *Int J Radiat Res*. 2016;14(4):379.

80. Ramdani N. Thermosetting micro-and nanocomposites for neutron radiation shielding. In: *Micro and Nanostructured Composite Materials for Neutron Shielding Applications*. Elsevier; 2020:83-123.
81. Shinn JF. Changes to Tensile Strength and Electromagnetic Shielding Effectiveness in Neutron Irradiated Carbon Nanocomposites. 2013.
82. TEKİN H, SİNGH V, Ümit K, MANICI T, ALTINSOY E. Investigation of nanoparticle effect on radiation shielding property using Monte Carlo method. *Celal Bayar Üniversitesi Fen Bilim Derg.* 2016;12(2).
83. Mansour A, Sayyed MI, Mahmoud KA, Şakar E, Kovaleva EG. Modified halloysite minerals for radiation shielding purposes. *J Radiat Res Appl Sci.* 2020;13(1):94-101.
84. Ziegler JF, Biersack JP, Ziegler MD. The stopping and range of ions in matter. *SRIM* <http://www.srim.org>. 2009.
85. Blackmore EW. Operation of the TRIUMF (20-500 MeV) proton irradiation facility. In: *2000 IEEE Radiation Effects Data Workshop. Workshop Record. Held in Conjunction with IEEE Nuclear and Space Radiation Effects Conference (Cat. No. 00TH8527)*. IEEE; 2000:1-5.
86. Blackmore EW, Evans B, Mouat M. Operation of the TRIUMF proton therapy facility. In: *Proceedings of the 1997 Particle Accelerator Conference (Cat. No. 97CH36167)*. Vol 3. IEEE; 1997:3831-3833.
87. Blackmore EW, Dodd PE, Shaneyfelt MR. Improved capabilities for proton and neutron irradiations at TRIUMF. In: *2003 IEEE Radiation Effects Data Workshop*. IEEE; 2003:149-155.
88. Roy SC, Sandison GA. Scattered neutron dose equivalent to a fetus from proton therapy of the mother. *RaPC.* 2004;71(3-4):997-998.
89. Eaton BR, MacDonald SM, Yock TI, Tarbell NJ. Secondary malignancy risk following proton radiation therapy. *Front Oncol.* 2015;5:261.
90. Wang B, Xu XG, Goorley JT, Bozkurt A. Issues related to the use of MCNP code for an extremely large voxel model VIP-Man. In: *American Nuclear Society Topical Meeting, Chattanooga, Tennessee. LaGrange Park, IL: American Nuclear Society.* ; 2005.
91. Caracappa PF, Rhodes A, Fiedler D. Multi-resolution voxel phantom modeling: a high-resolution eye model for computational dosimetry. *Phys Med Biol.* 2014;59(18):5261.
92. Weber S. Nanotube Modeler. 2018. <http://www.jcrystal.com/products/wincnt/index.htm>.
93. Radiation weighting factor. Health Physics Society. <http://hps.org/publicinformation/radterms/radfact122.html>. Accessed October 2, 2020.

94. Radiation PAN. NCRP-38. *Natl Counc Radiat Prot Meas Washington, DC.* 1971.
95. Kerr GD, Fix JJ. *Technical Basis for Conversion from NCRP Report 38 Neutron Quality Factors to ICRP Publication 60 Radiation Weighting Factors for Respective IREP Input Neutron Energy Ranges.*; 2006.

Appendices

Appendix A – SRIM Output for Hydrogen in Brass

***Output has been truncated to show only 105 MeV proton range**

=====

SRIM version ---> SRIM-2013.00

Calc. date ---> August 27, 2020

=====

Disk File Name = SRIM Outputs\Hydrogen in Cu-Zn-Pb-105MeV.txt

Ion = Hydrogen [1] , Mass = 1.008 amu

Target Density = 8.4900E+00 g/cm3 = 6.5109E+22 atoms/cm3

===== Target Composition =====

Atom	Atom	Atomic	Mass
Name	Numb	Percent	Percent
----	----	-----	-----
Cu	29	056.67	045.86
Zn	30	033.33	027.75
Pb	82	010.00	026.39

=====

Bragg Correction = 0.00%

Stopping Units = MeV / (mg/cm2)

Ion	dE/dx	dE/dx	Projected	Longitudinal	Lateral
Energy	Elec.	Nuclear	Range	Stragging	Stragging
-----	-----	-----	-----	-----	-----
105.00 MeV	4.363E-03	1.524E-06	16.25 mm	772.09 um	1.09 mm

=====

Appendix B – MCNP Input Decks

Bulk Composite Input Deck

Bulk Composite - 63 MeV Input Dck

```

c      CELL CARDS
c      matl $  dens  bounding surfaces
1      5      -11.34 -2          imp:n=1 imp:h=1      $lead scatterer
2      3      -8.49  -3 4       imp:n=1 imp:h=1      $collimator 1
3      4      -0.00225 -5       imp:n=1 imp:h=1      $DIC
4      2      -1.18  -6         imp:n=1 imp:h=1      $RS
5      3      -8.49  -7 8       imp:n=1 imp:h=1      $collimator 2
c      -----nanocomposite-----
6      1      -1.038 -9         imp:n=1 imp:h=1      $sample
c      -----
10     4      -0.00225 -13       imp:n=1 imp:h=1      $BIC
11     4      -0.00225 -1 2 5 6 9 13 #2 #5  imp:n=1 imp:h=1      $outer box
12     0              1         imp:n=0 imp:h=0      $void
c      END OF CELL CARDS

c      SURFACE CARDS
1      BOX  -37.600034 -5 -5     121 0 0 0 10 0 0 0 10      $outer box
2      BOX  -31.601034 -4 -4     0.001 0 0 0 8 0 0 0 8      $lead scatterer
3      BOX  -31.600034 -4 -4     1.00 0 0 0 8 0 0 0 8      $box of collimator 1
4      RCC  -31.600034 0 0       1.00 0 0 0.6              $inner cylinder of collimator 1
5      BOX  -30.600034 -4 -4     1.00 0 0 0 8 0 0 0 8      $DIC
6      BOX  -21.600034 -4 -4     2.05 0 0 0 8 0 0 0 8      $RS
7      BOX  -1.000034 -4 -4     1.00 0 0 0 8 0 0 0 8      $box of collimator 2
8      RCC  -1.000034 0 0       1.00 0 0 0.95             $inner cylinder of collimator 2
c      -----nanocomposite-----
9      BOX  -3.4E-5 -3.4E-5 -1.25E-2 6.8E-5 0 0 0 6.8E-5 0 0 0 2.5E-2  $sample
c      -----
13     BOX  75.899966 -4 -4     1.00 0 0 0 8 0 0 0 8      $BIC
c      END OF SURFACE CARDS

c      DATA CARDS
MODE H N
PHYS:H 100
PHYS:N 100
CUT:H J 3.0
SDEF POS= -36.600034 0 0  AXS= 1 0 0  ERG= 63  VEC= 1 0 0  DIR= 1.0
PAR= HRAD= D1  EXT= 0
SI1 0 5E-5  $radial sampling from 0 to max radius
SP1 -21 1  $-21=power law: p(x)=c|x|^a, here a=1
c      proton dose tally
F6:H 3 10
FC6 PRIMARY PROTONS
FM6 1.602e-10  $weighting factor (Gy/s/starting particle)
c      neutron dose tally
F4:N 3 10
FC4 SECONDARY NEUTRONS
DF4 iu=2 ic=20  $dose function card
FM4 2.7778e-4  $weighting factor (Sv/s/starting particle)
c      MATERIALS

```

M1	1001	0.595838	\$sample hydrogen
	6012	0.205549	\$sample carbon
	8016	0.099306	\$sample oxygen
	14028	0.099306	\$sample silicon
	hlib=.24h		
M2	6012	0.33333	\$lucite carbon
	1001	0.53333	\$lucite hydrogen
	8016	0.13334	\$lucite oxygen
	hlib=.24h		
M3	29063	-0.4253955	\$brass copper
	29065	-0.1896945	
	30000	-0.352	\$brass zinc
	82208	-0.017442	\$brass lead
	82206	-0.008103	
	82207	-0.007443	
	hlib=.24h		
M4	7014	-0.755267	\$air nitrogen
	8016	-0.231781	\$air oxygen
	6012	-0.0000124	\$air carbon
	hlib=.24h		
M5	82207	1	\$lead
	hlib=.24h		
NPS	3000000		
c	End of data cards		
c	END		

Appendix C – Nanotube Modeler

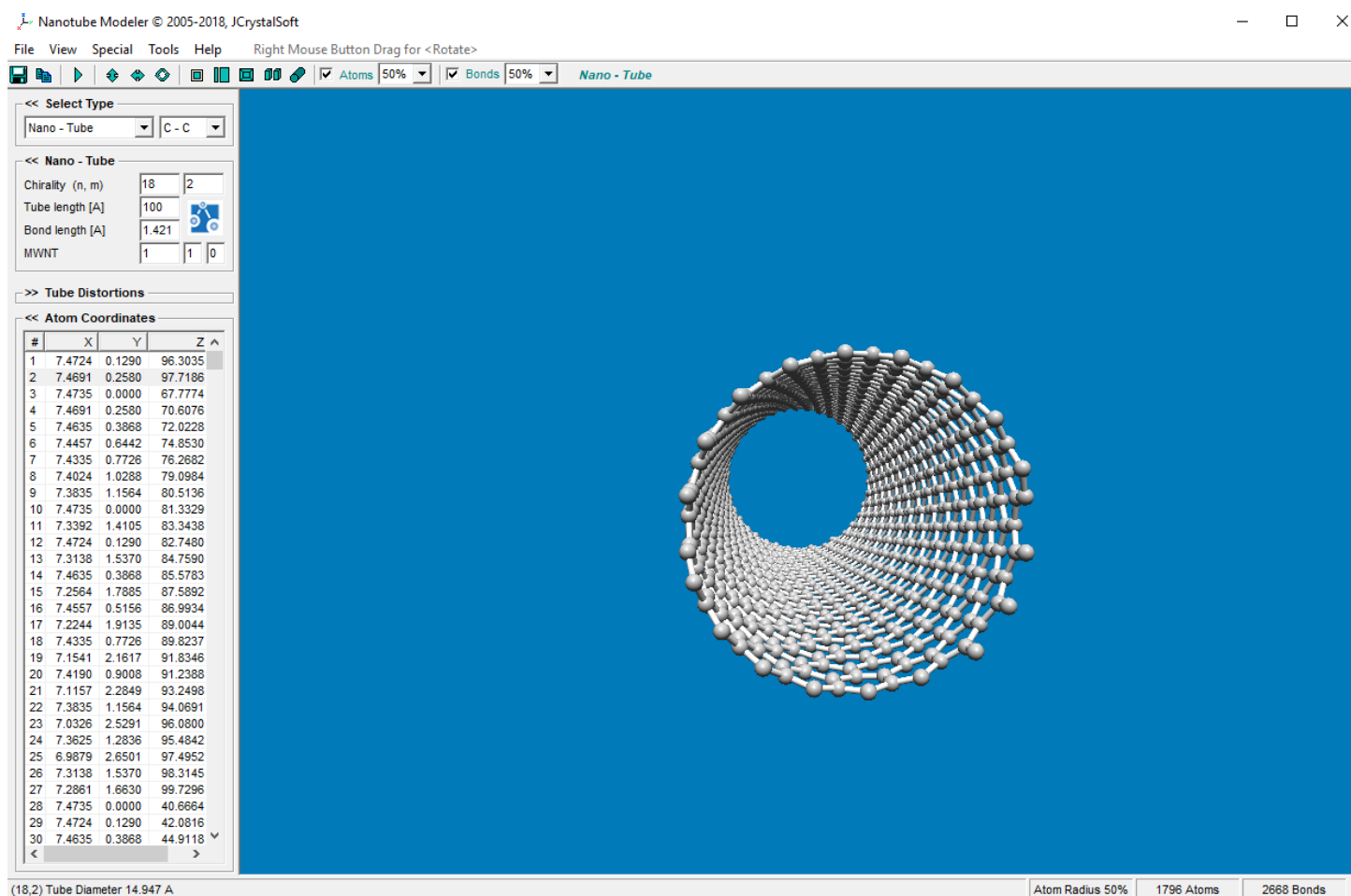


Figure C.1. Screen capture of Nanotube Modeler software, showing nanotube characteristics and atom coordinates on the left and a 3D visual of the nanotube on the right.

Appendix D – Python Scripts

RS Designation Script

```

1 #expand.py
2
3 import shutil
4
5 step = 20
6 start = 1800 + step
7 stop = 3400 + step
8
9 template = "C:/Users/Public/Al_105/1800.txt"
10
11 for x in range(start,stop,step):
12     fname = ("C:/Users/Public/Al_105/"+ str(x) + ".txt")
13     shutil.copy(template,fname)
14
15     num = x/1000.00
16     readable = open (fname, "r")
17     new_content = ""
18     for line in readable:
19         new = line.replace('1.800',str(num))
20         new_content += new
21     readable.close()
22
23     writeable = open(fname,'w')
24     writeable.write(new_content)
25     writeable.close()

```

Figure D.1. Screen capture of Python script used to write input files with designated RS values.

MCNP Run Command Script

```

1 #folder_run.py
2
3 import glob
4 import os
5
6 list = glob.glob('C:/Users/Public/Al_105/*.txt')
7
8 for x in range(0, len(list)):
9     fname = list[x]
10    RS = fname[-8:]
11    os.system('mcnp6 N='+RS)
12    print(RS+"complete")

```

Figure D.2. Screen capture of Python script used to sequentially run MCNP6 for all .txt files within a designated folder.

Data Extraction Script

```

1 #extract.py
2
3 import glob
4 import csv
5
6 path = "C:/Users/Justina Freilich/Desktop/Li2013/bulk/v2/"
7 filename = "v2.csv"
8 list = glob.glob(path + '*.txto')
9 rsname = ["RS"]
10 cell2h = ["DIC H"]
11 err2h = ["DIC H err"]
12 cell5h = ["BIC H"]
13 err5h = ["BIC H err"]
14 cell2n = ["DIC N"]
15 err2n = ["DIC N err"]
16 cell5n = ["BIC N"]
17 err5n = ["BIC N err"]
18 ratio = ["BIC/DIC"]
19 pdf4 = ["tally 4 stats"]
20 pdf6 = ["tally 6 stats"]
21
22 length = []
23 for x in range(0, len(list)):
24     fname = list[x]
25     length.append(len(fname))
26 for x in range(0, len(list)):
27     fname = list[x]
28     if len(fname) == max(length):
29         RS = fname[-9:-5]
30     else:
31         RS = fname[-8:-5]
32     rsname.append(RS)
33     lines = []
34     with open (list[x], "rt") as file:
35         for line in file:
36             lines.append(line.rstrip("\n"))
37     file.close()
38     sub_cell2 = "cell 3"
39     sub_cell5 = "cell 10"
40     counter = 0
41     index2 = []
42     index5 = []
43     for line in lines:
44         counter = counter + 1
45         if sub_cell2 in line:
46             index2.append(counter)
47         if sub_cell5 in line:
48             index5.append(counter)
49     print(index2,index5,RS)
50     Y2h = (lines[max(index2)])
51     error2h = float(Y2h[-6:])
52     value2h = float(Y2h[:-7])
53     Y2n = (lines[min(index2)])
54     error2n = float(Y2n[-6:])
55     value2n = float(Y2n[:-7])
56     cell2h.append(value2h)
57     err2h.append(error2h)
58     cell2n.append(value2n)
59     err2n.append(error2n)
60     Y5h = (lines[max(index5)])
61     error5h = float(Y5h[-6:])
62     value5h = float(Y5h[:-7])
63     Y5n = (lines[min(index5)])
64     error5n = float(Y5n[-6:])
65     value5n = float(Y5n[:-7])
66     cell5h.append(value5h)
67     err5h.append(error5h)
68     cell5n.append(value5n)
69     err5n.append(error5n)
70     sub_cell = "pdf"
71     counter = 0
72     indexpdf = []
73     for line in lines:
74         counter = counter + 1
75         if sub_cell in line:
76             indexpdf.append(counter+4)
77     Y4pdf = (lines[min(indexpdf)])
78     Y6pdf = (lines[max(indexpdf)])
79     if "no" in Y4pdf:
80         pdf4.append("no")
81     else:
82         pdf4.append("yes")
83     if "no" in Y6pdf:
84         pdf6.append("no")
85     else:
86         pdf6.append("yes")
87     ratio.append((value5n + value5h)/(value2n + value2h))
88 rows = zip(rsname, cell2h, err2h, cell5h, err5h, cell2n, err2n, cell5n, err5n, ratio, pdf4, pdf6)
89 print(rsname, cell2h, err2h, cell5h, err5h, cell2n, err2n, cell5n, err5n, ratio, pdf4, pdf6)
90 with open(path + filename, 'w', newline='') as compile:
91     writer = csv.writer(compile)
92     for row in rows:
93         writer.writerow(row)

```

Figure D.3. Screen capture of Python script used to extract tally values and relative error values from MCNP output files within a designated folder.